Materials Today • Volume xxx, Number xx • xxxx 2020

ELSEVIER

A brief review of dynamic mechanical metamaterials for mechanical energy manipulation

Lingling Wu [1,2,4,†], Yong Wang [3,†], Kuochih Chuang [3], Fugen Wu [4], Qianxuan Wang [1], Weiqi Lin [1], Hanqing Jiang [2,*]

[1] College of Railway Engineering, Wuyi University, Jiangmen 529020, China
[2] School for Engineering of Matter, Transport and Energy, Arizona State University, Tempe, AZ 85287, USA
[3] Department of Engineering Mechanics, Zhejiang University, Hangzhou, Zhejiang 310027, China
[4] School of Materials and Energy, Guangdong University of Technology, 510006, China

In the past decades, many mechanical metamaterials with uncommon static properties have been reported. On the other hand, mechanical metamaterials possessing extraordinary dynamic performance, also referred to as acoustic/elastic metamaterials, have gained more and more attractions. Examples include acoustic cloaking metamaterials that can generate an invisible region for acoustic waves, zero-stiffness metamaterials that can isolate vibrating mechanical energy, origami-based metamaterials that can realize the directional transmission of elastic waves and so on. To better understand the mechanisms adopted in dynamic mechanical metamaterials and present a general view about the existing works, we have reviewed some representative works and categorized them based on the ways of how these mechanical metamaterials manipulate the interactions between matters and mechanical energy. To distinguish the different categories of the dynamic mechanical metamaterials, we use a pair of binary numbers to measure the changing states of the magnitude and direction of the energy flow, respectively. A summary of some research works with associated reference numbers is presented in this paper with emphasis on the operating frequency, working bandwidth, and characteristic size of the element.

Keywords: Mechanical metamaterials; Energy manipulation; Phononic crystal; Local resonance

Introduction

Mechanical metamaterials [1–4], i.e., artificial materials elaborately designed to achieve unusual *apparent* mechanical performance, have been extensively investigated in recent decades. The objective performance includes unusual static behaviors (e.g., negative thermal expansion [5], negative Poisson's ratio [6] and so on [1]) and extraordinary dynamic behaviors (such as acoustic wave transmission with expected bandgaps or propagation paths [7–11], a unique combination of stiffness, strength and energy absorption performance [12], full-band mechanical vibration isolation [13], and other behaviors [14–16]). Microstructural design to obtain objective applications occupies the central position in the field of mechanical metamaterials. Design approaches and practical (or potential) applications, however, are versatile and are not appropriate to adopt as classification criteria. Ultimately, the microstructure design of dynamic mechanical metamaterials is to intervene the interaction between matter and energy, i.e., modifying the matter distribution to manipulate energy propagation. As a vector field, the *apparent* energy flow possesses two fundamental elements, i.e., the magnitude and flow direction. It is reasonable to classify dynamic mechanical metamaterials according to whether the magnitude and/or the flow direction of the *apparent* energy flow are changed.

Here, we use a pair of binary numbers (*a b*) to distinguish the different categories of the dynamic mechanical metamaterials. *a*

* Corresponding author.
E-mail address: Jiang, H. (hanqing.jiang@asu.edu)
† These authors contributed equally to this paper.

 https://doi.org/10.1016/j.mattod.2020.10.006

Please cite this article in press as: L. Wu et al., Materials Today, (2020), https://doi.org/10.1016/j.mattod.2020.10.006

and *b* measure the *apparent* changing states of the magnitude and direction of the energy flow, respectively, with value 0 meaning not change while value 1 meaning change. For instance, (0 1) means that after passing through the metamaterial, the magnitude of the energy flow does not change, while the direction changes (the deflection angle α takes the value from the semi-closed interval $(0, \pi]$). In the same way, (0 0) means that both the magnitude and direction of the energy flow remains unchanged; (1 0) means that only the magnitude changes, while the direction remains the same as before; and (1 1) means that both the magnitude and direction change after propagating through the metamaterial. A schematic of the energy flow propagating through four categories of the dynamic mechanical metamaterials is shown in Fig. 1, in which the thickness of streamlines represents the magnitude of energy flow.

Most existing researches on dynamic metamaterials belong to these four categories. For instance, as the acoustic wave transmits through an acoustic cloak, neither the magnitude nor the direction of the energy flow changes [17–49], and an acoustically invisible area could be created inside the metamaterial. On the other hand, for most vibration-isolation metamaterials, the magnitude of the energy flow will be suppressed after transmitting through them, while the direction remains unchanged [50–53]. Additionally, many acoustic lenses, such as the Luneburg lens [8,54–57] and Eaton lens [58,59], could deflect the direction of the energy flow without affecting the magnitude at least in theory. Ideal acoustic waveguides [60–64] could also reroute or program the propagation path of the energy flow while keeping the magnitude constant. Finally, acoustic black holes [65–67] bend the direction of waves and dissipate or absorb part of the energy simultaneously.

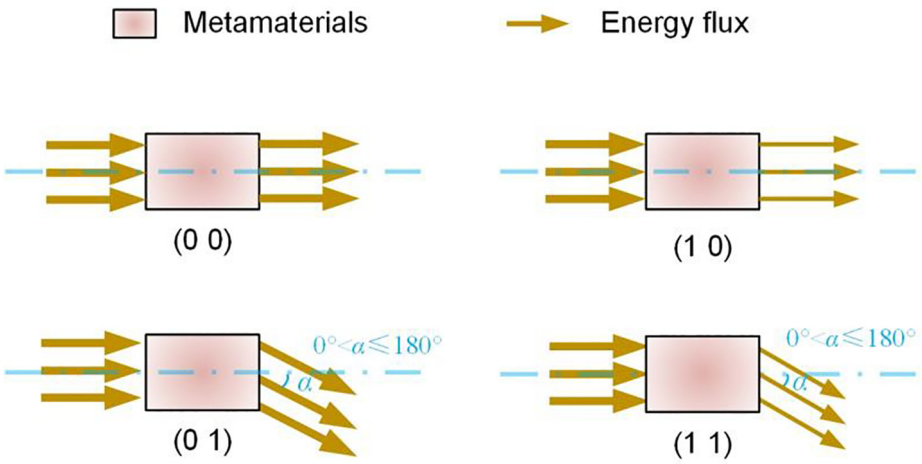

FIGURE 1

Four categories of dynamic mechanical metamaterials according to the manipulation of magnitude and direction of energy flow. The thickness of the streamlines represent the magnitude of energy flow.

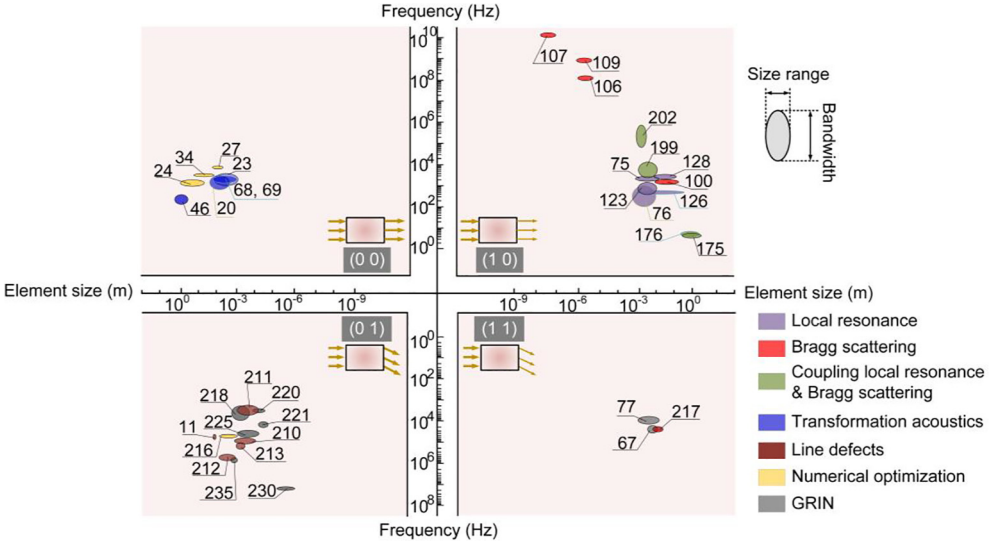

FIGURE 2

A brief summary of some existing research work according to the manipulation of magnitude or direction of energy flow. The horizontal and vertical axis shows the feature size of the element and frequency, respectively. The vertical geometry of the circles represents the working frequency band while their horizontal size shows the element size range. Different filling color of the circle illustrates different mechanism adopting in the reported works. To achieve a clearer presentation, we adopt the logarithmic coordinate for the vertical axis.

Please cite this article in press as: L. Wu et al., Materials Today, (2020), https://doi.org/10.1016/j.mattod.2020.10.006

To better illustrate the correspondence between these categories of the dynamic mechanical metamaterials and the application aspects, a summary of some existing works with associated reference numbers is roughly presented in Fig. 2, with emphasis on the operating frequency, working bandwidth, and characteristic size of a unit cell. The horizontal axis indicates the feature size of the elements, and the vertical axis shows the effective frequency range. Each work is represented by an ellipse with the horizontal semi-axis being the range of feature size and the vertical semi-axis being the effective working bandwidth.

In Section 1, we provide some representative applications for these four categories. Then, by analyzing the physical mechanisms utilized in these applications, we refine the fundamental mechanisms behind various functions, and those in charge of adjusting the magnitude of the energy flow are presented in Section 2, while those responsible for the change of the flow direction are discussed in Section 3. In both sections, the physical mechanisms, typical structures, and regulatory mechanisms of existing works are explained in detail. Finally, we summarize the existing problems and provide the possible solutions and the future opportunities for the development of dynamic mechanical metamaterials. We believe this review can provide some guidance for designing novel dynamic metamaterials.

Representative applications of these four categories

Class (0 0): acoustic cloaking

Class (0 0) of dynamic mechanical metamaterials neither changes the magnitude nor changes the flow direction of the outlet energy flow compared with the inlet one, which corresponds exactly to ideal acoustic cloaks providing an invisible area for acoustic waves [23,24,27,34,42,46,47,49,68,69]. Although the wave is guided around the cloaking area by the anisotropic distribution of effective elastic parameters, the final direction of energy flow doesn't change after propagating through the metamaterial. By manually creating the gradient distribution of elastic parameters, acoustic waves will not change the magnitude or the propagating direction after propagating through the cloaking area. Typical acoustic cloaks fabricated for practical applications are presented in Fig. 3, where the acoustic cloaks can effectively bend sound waves around hidden objects with reduced scattering and shadows. Fig. 3(a) shows an acoustic cloak [46] with a concentric alternating layered structure designed with homogeneous isotropic materials. Fig. 3(b) presents a 2D acoustic cloak [68] while Fig. 3(c) shows a 3D broadband acoustic cloak that renders a region of pyramidal space, which is three wavelengths in diameter, invisible to sound [69].

Class (1 0): mechanical energy barriers and isolators

The second application type is the use of mechanical metamaterials to control only the magnitude of the energy flow. To achieve this purpose, mechanical energy has to bedissipated [70–73], confined [74], or harvested and transferred to other forms [75,76] by the metamaterials. Typical structures are illustrated in Fig. 4. Fig. 4(a) [74] shows a broadband fractal acoustic metamaterial that can attenuate sounds at selective frequencies ranging from 225 Hz to 1175 Hz. Fig. 4(b) [76] shows an acoustically reflecting surface with hybrid resonances, and acoustic waves are absorbed or converted into other forms of the energy. Fig. 4(c) [73] shows a metamaterial with visco-thermal effects

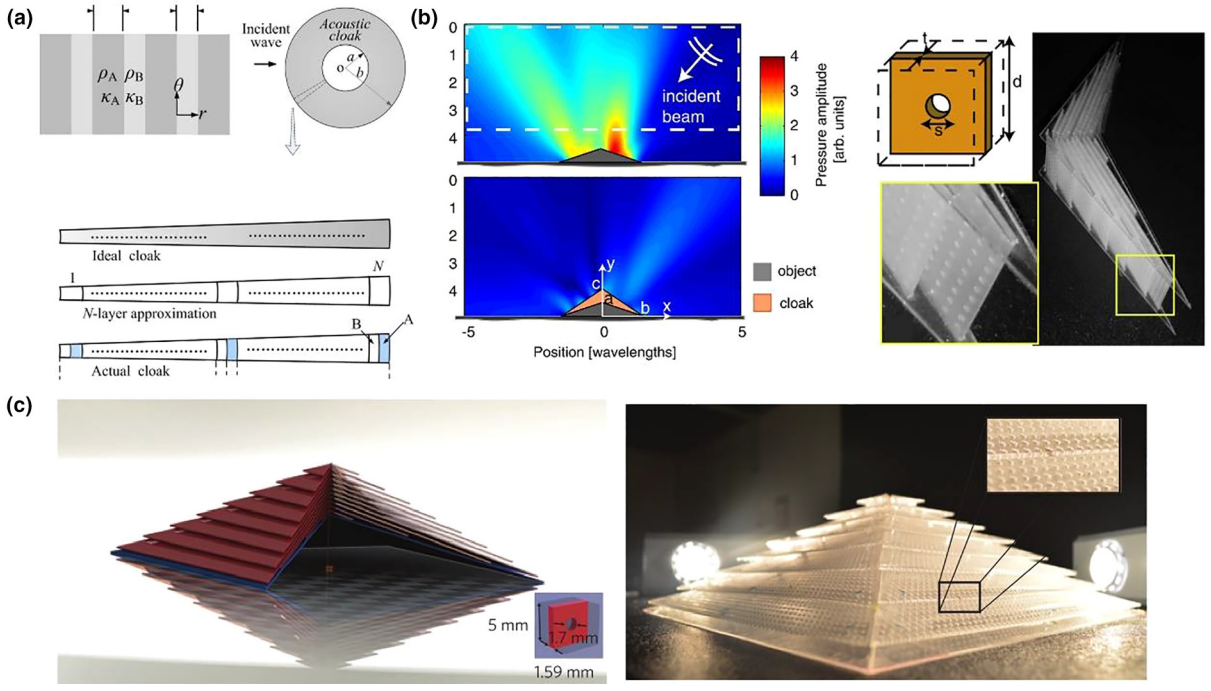

FIGURE 3

Realization of acoustic cloak. (a) Top: Structure of acoustic layered system (left) and schematic of an ideal 2D acoustic cloak (right). Bottom: The design procedure of the multilayered cloak. (Reprinted with permission from Ref. [46]. 2008, AIP Publishing.) (b) Left: Simulated acoustic field of a triangular object (top) and object covered by a cloak (bottom) placed on a reflecting horizontal surface. Right: Picture of the cloak sample. (Reprinted with permission from Ref. [68]. 2011, American Physical Society.) (c) Left: Physical structure of the designed cloak and unit-cell dimensions. Right: Photograph of the actual cloaked object, placed on the ground. (Reprinted with permission from Ref. [69]. 2014, Springer Nature.).

Please cite this article in press as: L. Wu et al., Materials Today, (2020), https://doi.org/10.1016/j.mattod.2020.10.006

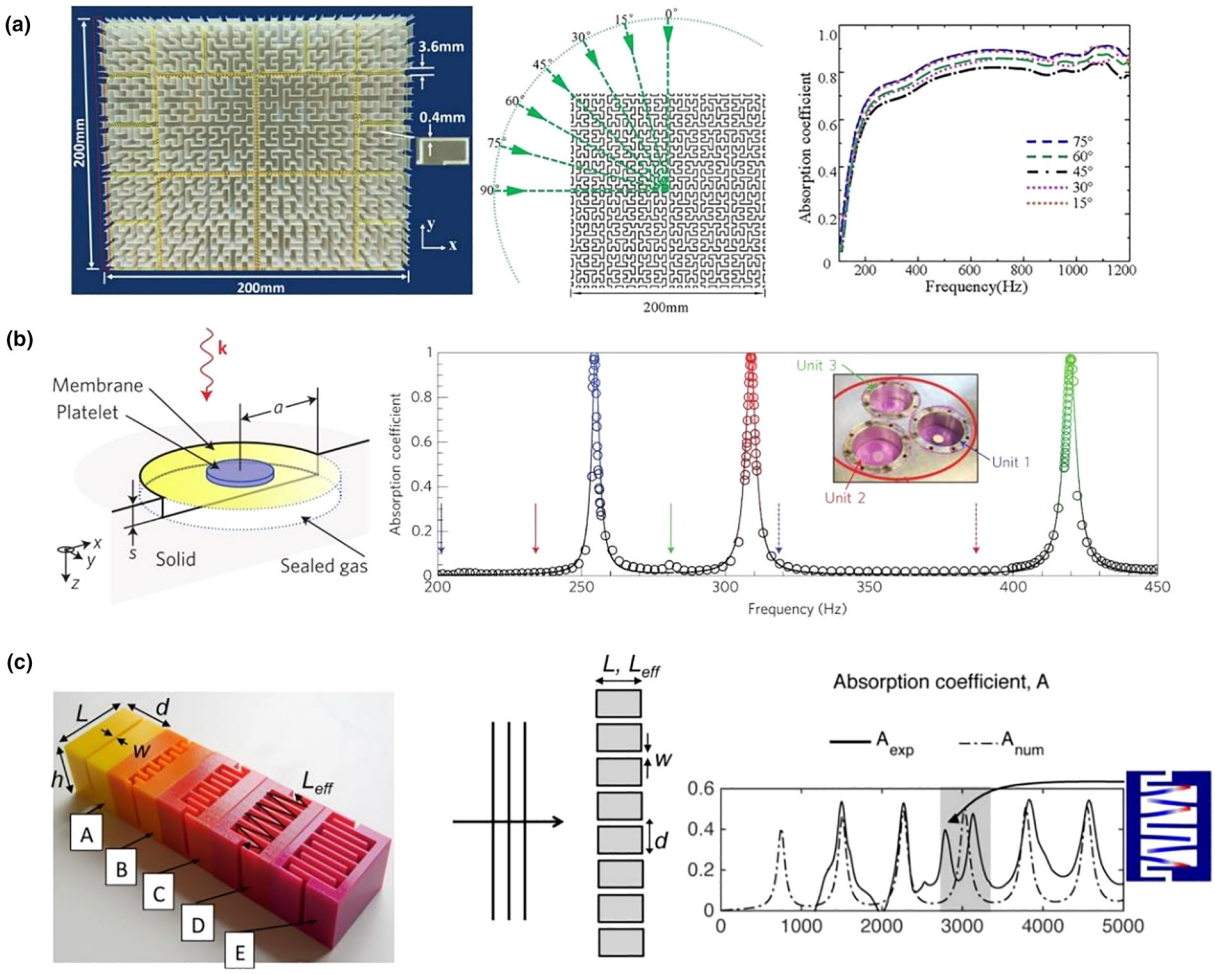

FIGURE 4

(a) Left: The prototype of a fabricated fractal acoustic metamaterial absorber. Middle: Schematic of the absorber at the incident angle of 15°, 30°,45°,60°, and 75°. Right: The simulated absorption coefficients for different incident angles. (Reprinted with permission from Ref. [74]. 2016, AIP Publishing.) (b) Left: Schematic illustration of a membrane acoustic metamaterial unit cell's components and geometry. Right: High (>0.99) absorption attained at tunable multiple frequencies. (Reprinted with permission from Ref. [76]. 2014, Springer Nature.) (c) Left: Fabricated metamaterial sample with visco-thermal effects. Middle: 2D perforated slab equivalent to the one studied experimentally. Right: the absorption coefficients for one of the metamaterials, where the shaded region represents the frequency range in which vibrational modes may exist. (Reprinted with permission from Ref. [73]. 2016, IOP Publishing.)

consisting of rigid slabs with slits embedded in air. At a specific geometrical parameter of the slit width, the energy will be highly dissipated.

Class (0 1): wave beam steering and wave guiding

In some applications, such as ultrasonic imaging systems, energy loss is not desired during the directional wave beam steering or wave guiding process. Only the direction change of the energy flow is required. Therefore, there should be no damping element in the system. Typical devices are shown in Fig. 5, where Fig. 5(a) shows an acoustic bending waveguide achieved by altering the index distribution [63]. The refractive indices of the medium can be discretized, and the discrete refractive indices are achieved by using a 2D gradient index (GRIN) sonic crystal. Fig. 5(b) shows an acoustic retroreflector [55] to reroute the incident waves back toward the source with minimal scattering.

Class (1 1): acoustic black hole

Acoustic black holes are introduced to control both the direction and magnitude of the energy flow simultaneously. Several examples of acoustic black holes are given in Fig. 6. Fig. 6(a) shows an acoustic black hole absorber made of acoustic metamaterials, which guides an incident acoustic wave into a central cavity spirally [67]. When beam is incident at an off-center position, the wavefront within the acoustic black hole is distorted and part of the energy flow winds spirally towards the center, which will be absorbed by the dissipative core. Fig. 6(b) shows a 2D omnidirectional acoustic absorber that can achieve the 98.6% absorption of acoustic waves in water, forming an effective acoustic black hole [77]. Similarly, this artificial black hole consists of an absorptive core coated with layers of periodically distributed polymer cylinders embedded in water.

Physical mechanisms to intervene in the magnitude of energy

Waves propagate in dynamic mechanical metamaterials only within specific frequency bands, referred to as pass bands, and they might be blocked within other frequency bands, which are called stopbands or bandgaps. The mechanisms of mechani-

Please cite this article in press as: L. Wu et al., Materials Today, (2020), https://doi.org/10.1016/j.mattod.2020.10.006

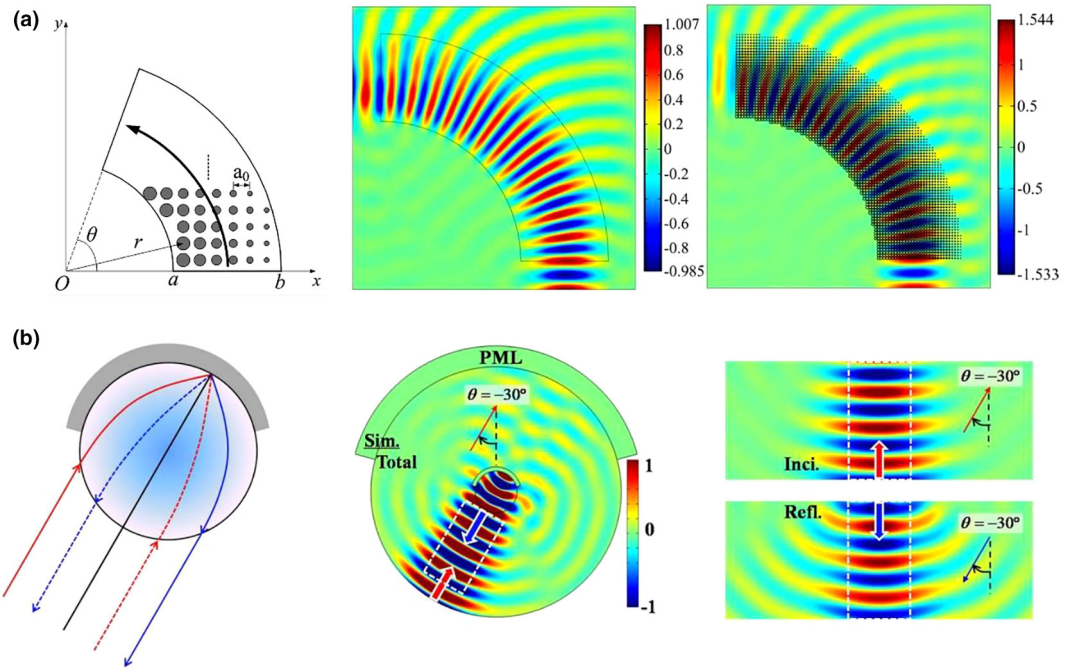

FIGURE 5

(a) Left: Schematic of the bending waveguide structure, where the bold solid line with arrow denotes the direction of wave propagation and the gray regions represent the square array of steel cylinders with spatially varying radii. Middle: Acoustic pressure field distribution for Finite-element-method simulations of the acoustic bending waveguide with the continuous refractive index variation. Right: Acoustic pressure field distribution of the graded sonic crystal approximation. (Reprinted with permission from Ref. [63]. 2011, AIP Publishing.) (b) Left: The schematic of an acoustic retroreflector composed of a Luneburg lens (gradient color) and a reflector (gray color). Middle: The simulated total acoustic pressure field of an ideal acoustic retroreflector for the incident beam with at a working frequency of 3.0 kHz. Right: The corresponding simulated acoustic pressure field patterns of the incident beam (the red arrow) toward the retroreflector and the reflected beam from the retroreflector (the blue arrow). (Reprinted with permission from Ref. [55]. 2018, American Physical Society.)

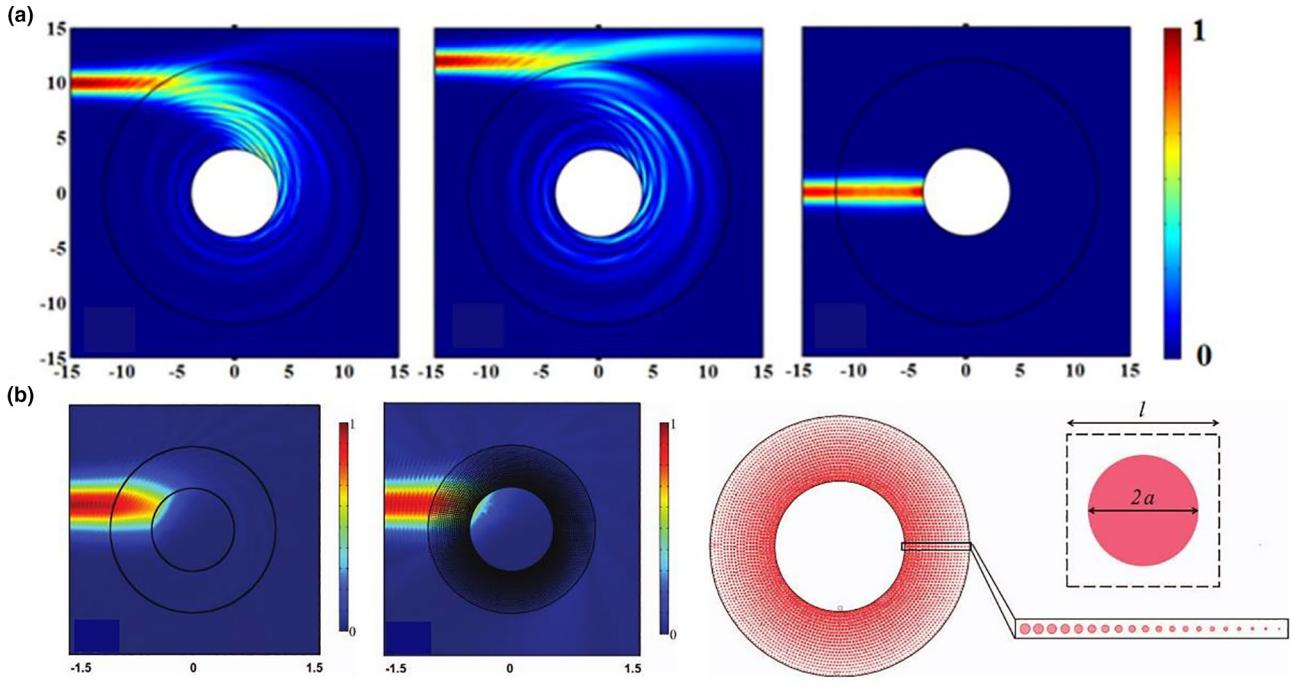

FIGURE 6

(a) Intensity fields when a Gaussian beam is incident on different regions of an acoustic black hole. Left: Beam is incident at a general position. Middle: Beam is tangential with the boundary. Right: Beam points to the center. The horizontal and vertical axes denote the distance in centimeter. (Reprinted with permission from Ref. [67]. 2011, AIP Publishing.) (b) Left: A Gaussian beam incident on an acoustic black hole that is on- and off-center. Right: A sketch of an artificial structure for an acoustic black hole. Right bottom: a close-up of the structure. The red structures are polymer cylindrical rods. Right above: the unit cell of the structure. (Reprinted with permission from Ref. [77]. 2013, AIP Publishing.)

Please cite this article in press as: L. Wu et al., Materials Today, (2020), https://doi.org/10.1016/j.mattod.2020.10.006

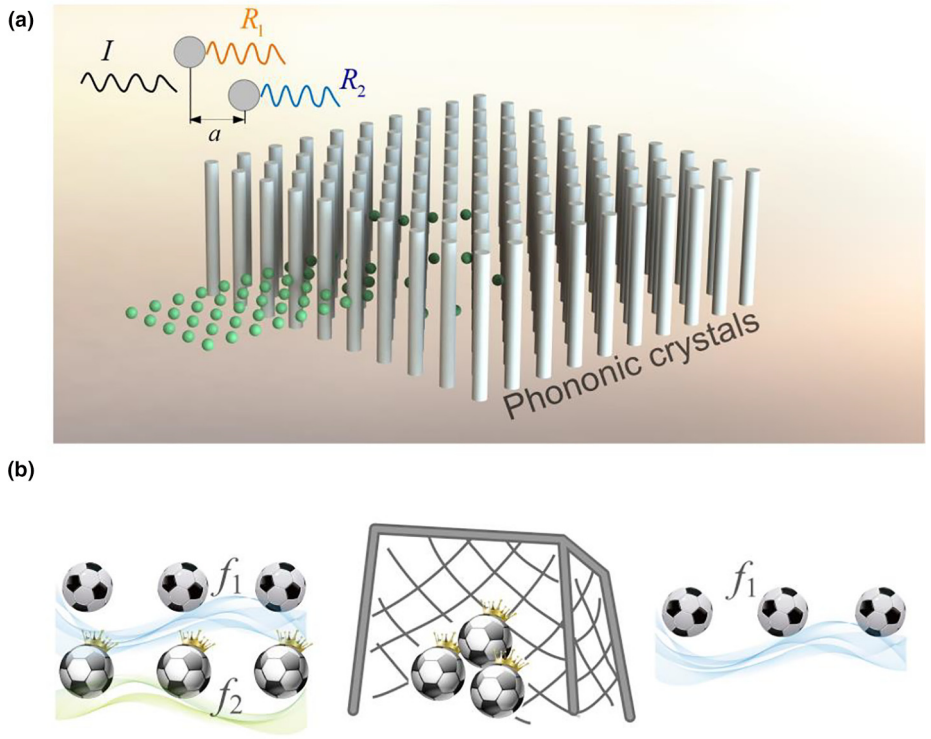

FIGURE 7

Schematic illustration of the (a) Bragg scattering and (b) local resonant mechanisms. The balls in both plots represents energy carried by waves with specific frequency. The structure in (a) describes a typical phononic crystal constructed by periodic solid inclusions embedded in air. Balls with a crown in (b) represent energy carried by wave f_2 in the bandgap range, while balls without a crown represent energy carried by wave f_1 in the passband region. The football goal in (b) represents metamaterials composed of resonant elements, that could trap energy carried by waves in the bandgap region.

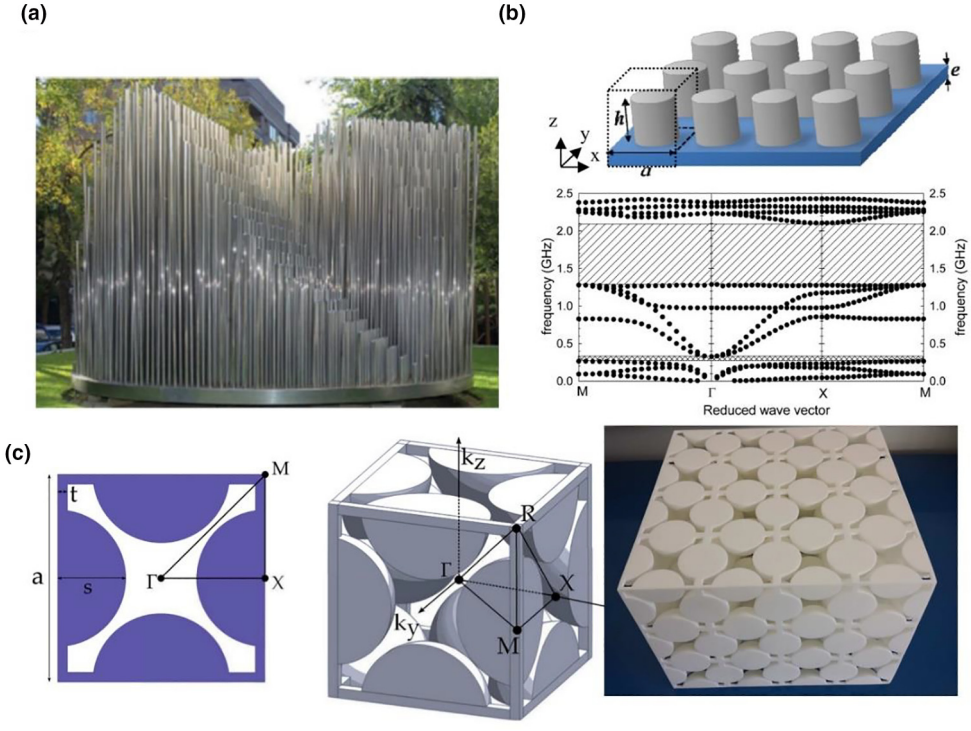

FIGURE 8

(a) Kinematic sculpture by Eusebio Sempere in Madrid consisting of a periodic distribution of hollow stainless-steel cylinders with a diameter of 2.9 cm, simple cubic symmetry and a unit cell of 10 cm. (Reprinted with permission from Ref. [100]. 1995, Springer Nature.) (b) Top: Phononic crystal made of a square lattice of finite cylinders deposited on a homogeneous plate. The dashed cube represents a unit cell of the periodic structure with dimensions (a, a, b). Bottom: Band structure in the frequency range [0, 2.5] GHz for steel cylinders on a silicon plate. (Reprinted with permission from Ref. [102]. 2009, John Wiley and Sons.) (c) Left and middle: Unit cell topology for a 3D phononic crystal. Right: Prototype of the finite crystal, composed by $4 \times 4 \times 3$ unit cells and made of Nylon PA2200 by additive manufacturing. (Reprinted with permission from Ref. [101]. 2016, AIP Publishing.)

Please cite this article in press as: L. Wu et al., Materials Today, (2020), https://doi.org/10.1016/j.mattod.2020.10.006

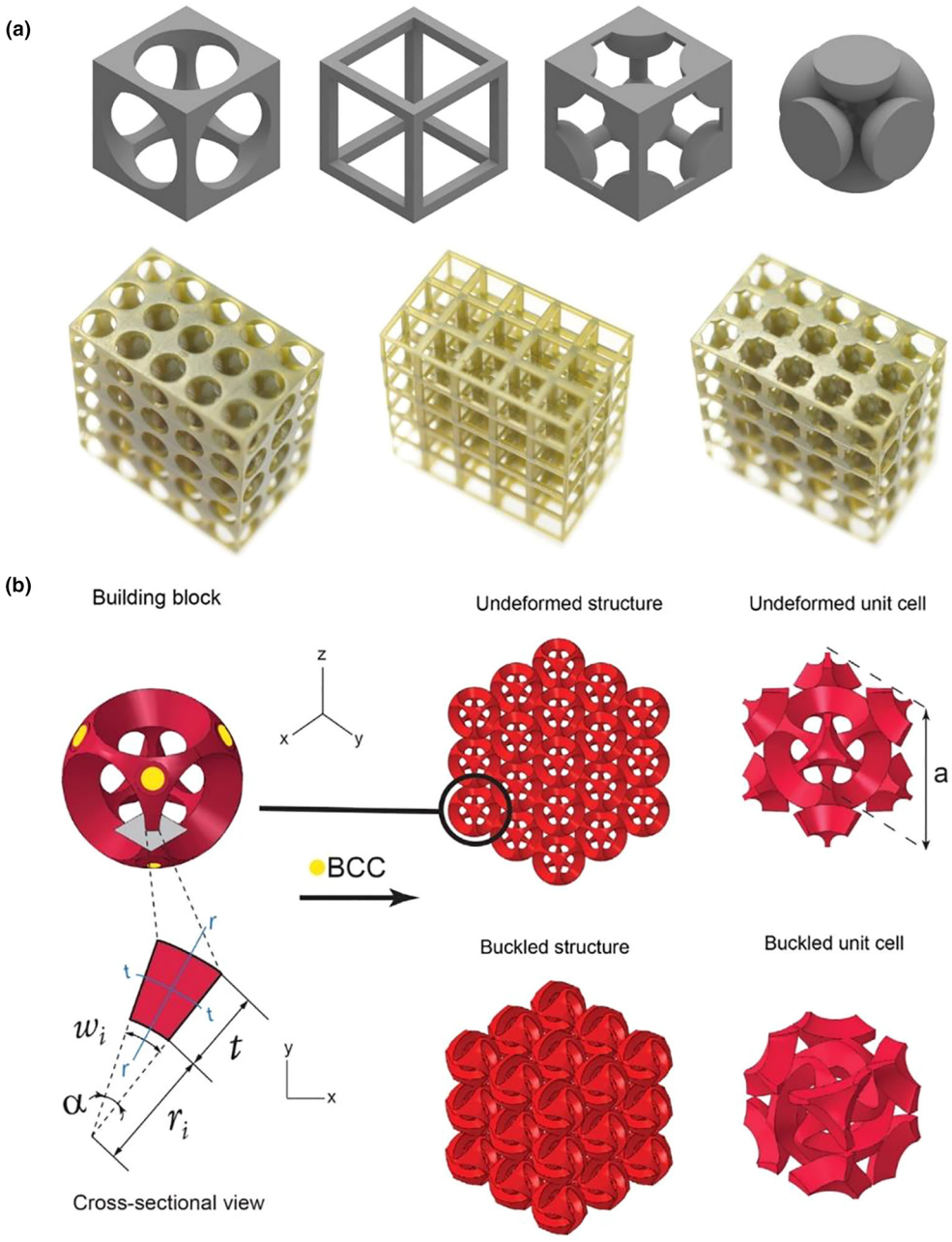

FIGURE 9

(a) Top: Exemplary cubic unit cell geometries. From left to right: Unit cell with three cylindrical holes, quadratic scaffold, corner balls connected by circular cylindrical beams, and face centered balls connected by quadratic beams. Bottom: Photographs of fabricated simple cubic phononic crystals with 3 mm lattice constant consisting of three cylindrical holes (left); rectangular scaffold (middle); and corner balls connected by cylindrical beams (right). (Reprinted from Ref. [103]) (b) Tunable 3D phononic crystal composed of a periodic array of structured shells arranged to form a body-centered cubic lattice. When compressed, this structure undergoes an instability, which results in folding of all the building blocks. (Reprinted with permission from Ref. [104]. 2015, AIP Publishing.)

cal metamaterials to intervene in the magnitude of mechanical waves strongly depend on their microstructure and could be divided into two main different phenomena at the micro-level [78]:

① Bragg scattering: The propagating wave is prohibited at specific wavelengths corresponding to the characteristic size of the microstructure (i.e., unit cells) of the metamaterials. In the electromagnetic area, periodic structures that possess bandgaps to prevent light propagation are called photonic crystals and have been widely investigated for decades. Similarly, mechanical waves propagating in metamaterials with specific microstructures also present bandgap characteristics. To explain the underlying physics of the interaction between waves and microstructures, researchers proposed a generalized continuum

Please cite this article in press as: L. Wu et al., Materials Today, (2020), https://doi.org/10.1016/j.mattod.2020.10.006

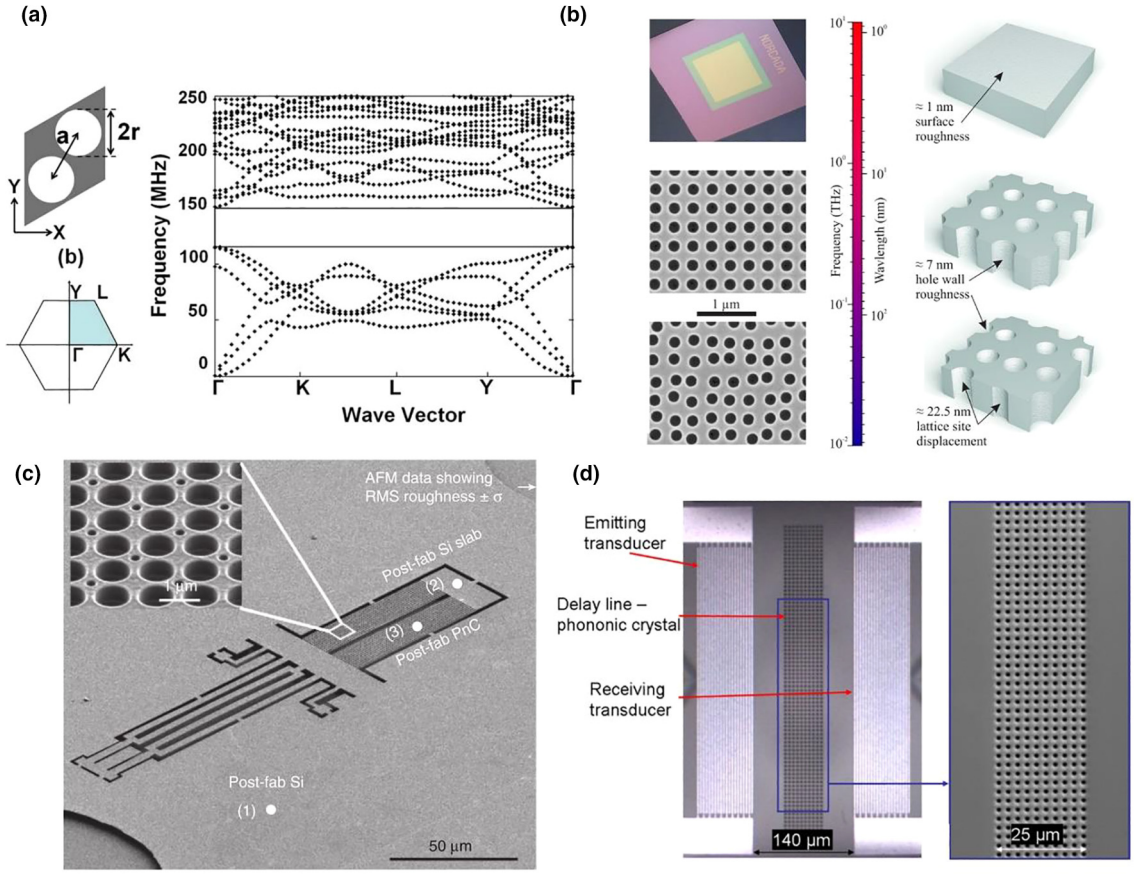

FIGURE 10

(a) Left: A unit cell and the irreducible part of the Brillouin zone for hexagonal lattice in Si. Right: Band structure of the hexagonal phononic crystal plate. (Reprinted with permission from Ref. [106]. 2008, AIP Publishing.) (b) Optical image of a 250 nm thick Si membrane with ordered and disordered phononic crystal with equal hole diameter and filling fraction of 0.267. (Reprinted with permission from Ref. [107]. 2016, American Chemical Society.) (c) SEM image of a phononic crystal matrix sample. (Reprinted with permission from Ref. [108]. 2015, Springer Nature.) (d) Optical photograph of a phononic crystal delay line and the phononic crystal region. (Reprinted with permission from Ref. [109]. 2011, AIP Publishing.)

model [78–83] named as relaxed micromorphic, which could explain the microstructure-related frequency band-gaps in the context of macroscopic continuum mechanics [82].

② Local resonance: arranging resonators (normally periodically) to suppress waves at the resonant frequencies of the resonators. The mechanical energy will be confined inside the metamaterial, and a macroscale stopband will be created. Local resonators are originally investigated in the Maxwell–Rayleigh model [84]. Various continuous models, including extensional rods, Euler and Timoshenko beams [85] and so on have been discussed to illustrate the dynamic behaviors of materials containing local resonators [86].

Here, we present the physical schematic of the two mechanisms in a metaphorical way as shown in Fig. 7, where the energy flow carried by waves could be analogous to balls to give a better understanding.

Fig. 7(a) explains the Bragg scattering process. To simplify the explanation, we assume that the incident wave is in the form of:

$$I = \cos(kx - \omega t) \tag{1}$$

where $\omega = \frac{2\pi}{T}$ is the angular frequency corresponding to period T and k represents the wave vector. When the traveling wave is transmitted to a scatterer, the scatterer will radiate waves with a phase difference $\Delta\varphi$. As shown in Fig. 7(a), when two identical scatterers are considered, the radiated waves are expressed as follows:

$$R_1 = \cos(kx - \omega t + \Delta\varphi) \tag{2}$$

$$R_2 = \cos(kx - \omega t + \Delta\varphi + ka) \tag{3}$$

It is well known that two waves with phase differences will interfere with each other. Therefore, when $ka = \pi$, there will be a strong destructive effect on the propagation of waves; i.e., Bragg scattering occurs. For periodic distributed scatterers that meet this condition, a bandgap will open where waves with the corresponding wavelength cannot propagate. The periodic elastic material possessing bandgap performance is called a phononic crystal by analogy to a photonic crystal [87]. From the Bragg scattering mechanism, we can easily understand that the bandgap is closely related to the periodicity of the structure and dependent on the lattice constant a, which is completely different from the local resonant mechanism shown in Fig. 7(b). To better illustrate the mechanism of local resonators, the resonator element can be assumed to a football goal that could trap the energy "balls" carried by waves within bandgap range. By contrast, if the frequency falls in the passband region, energy carried by the wave will propagate through the metamaterial. Therefore,

Please cite this article in press as: L. Wu et al., Materials Today, (2020), https://doi.org/10.1016/j.mattod.2020.10.006

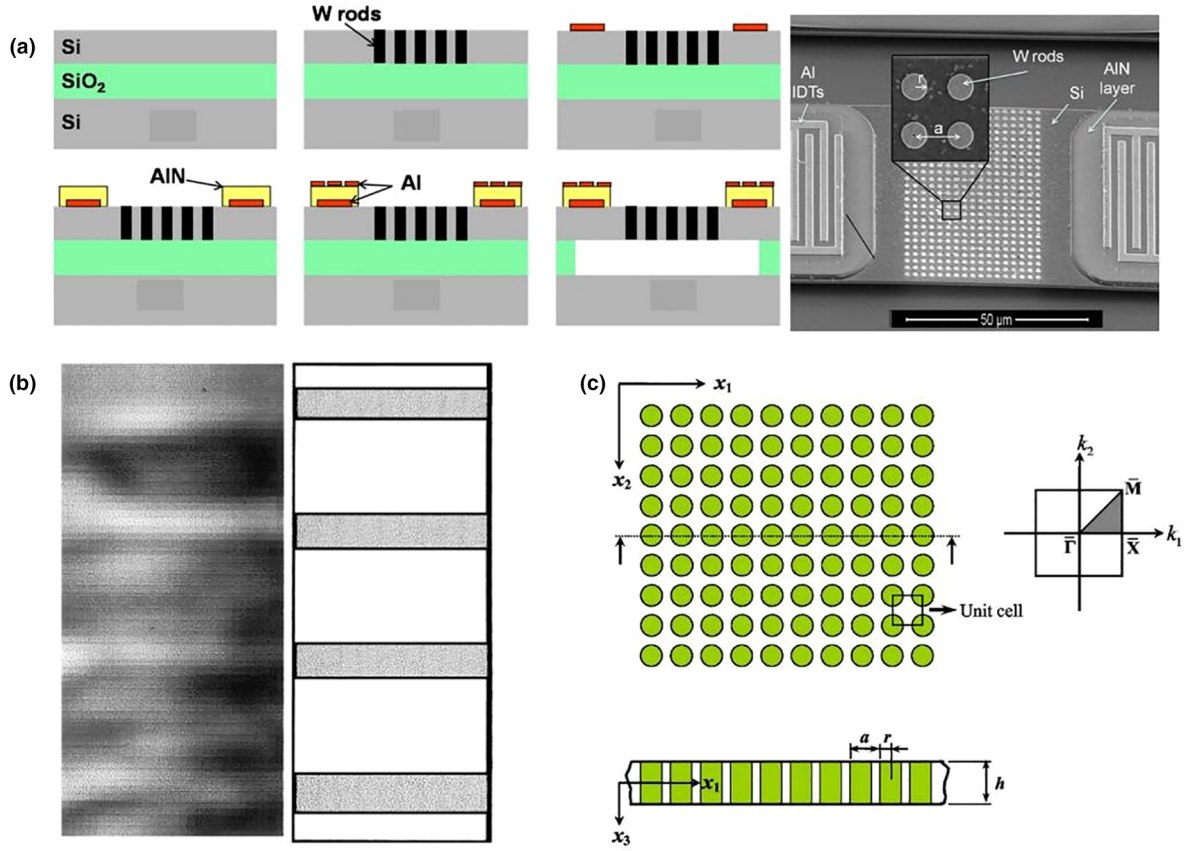

FIGURE 11

(a) Left: Fabrication process for the WSi phononic crystal. Right: An SEM image showing the phononic crystal and AlN transducers. (Reprinted with permission from Ref. [110]. 2010, AIP Publishing.) (b) Vibration amplitude scans in the [100] direction for an aluminum alloy plate with a square periodic arrangement of cylindrical holes filled with mercury. (Reprinted with permission from Ref. [111]. 1998, American Physical Society.) (c) Top view and cross-section of an infinite two-dimensional phononic crystal plate composed of Au inclusions embedded in epoxy substrate. (Reprinted with permission from Ref. [112]. 2006, American Physical Society)

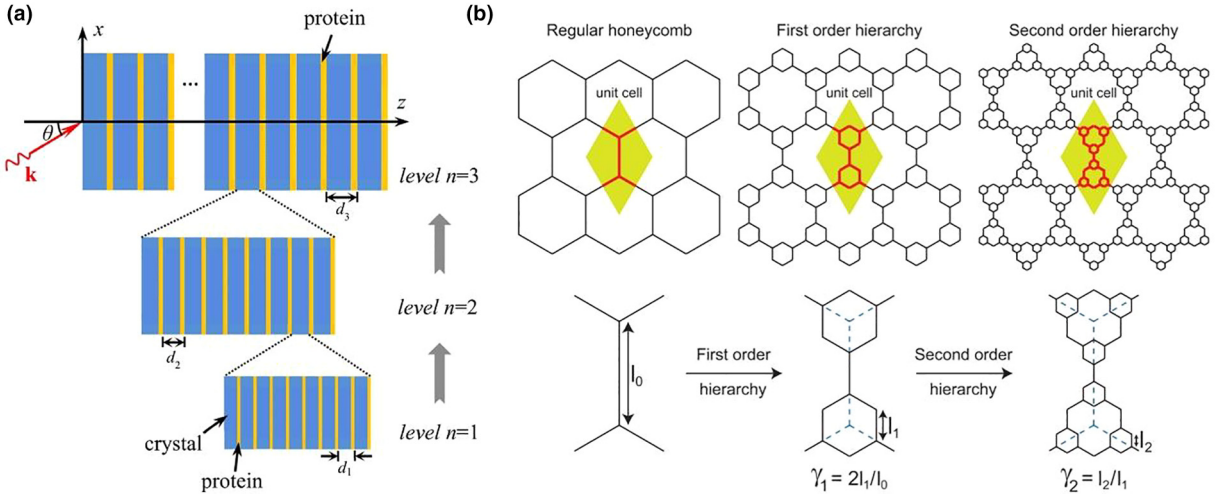

FIGURE 12

(a) Schematic illustration of the multilayered hierarchical structured model with 3 levels of hierarchy. The unit cell at each level of hierarchy is composed of a hard material layer and a soft layer. (Reprinted with permission from Ref. [113]. 2013, AIP Publishing.) (b) Top: The evolution of a regular hexagonal honeycomb (left) to first-order (middle) and second-order (right) hierarchical honeycombs. Bottom: Corresponding primitive unit cells of the structures. (Reprinted with permission from Ref. [114]. 2015, American Physical Society.)

Please cite this article in press as: L. Wu et al., Materials Today, (2020), https://doi.org/10.1016/j.mattod.2020.10.006

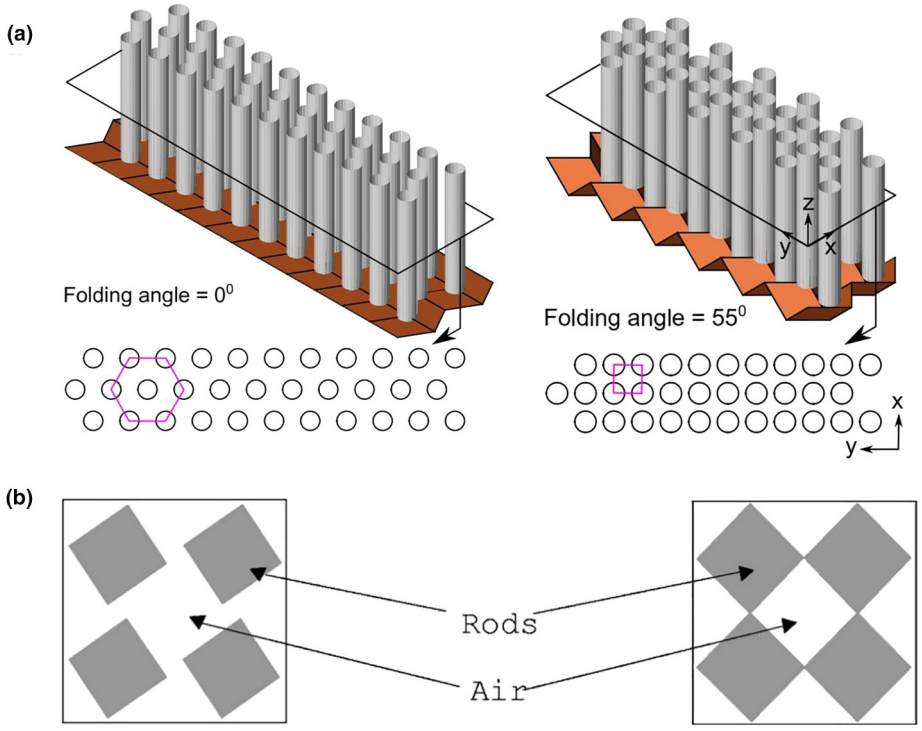

FIGURE 13

(a) Illustrations of different folding configurations of an origami sonic barrier and their corresponding cross-section views. The pink polygons in cross-section views identify different lattice patterns and show that the lattice transforms from a hexagon (left) to a square (right), when the folding angle is shifted from 0° to 55°. (Reprinted with permission from Ref. [116]. 2017, AIP Publishing) (b) The control of acoustic-frequency gaps by rotating the elements. Left: The filling fraction was set at 0.40, and the rotation angle as 35°. Right: The filling fraction is 0.50 and the rotation angle is 45°. (Reprinted with permission from Ref. [117]. 2001, American Physical Society.)

this mechanism does not rely on the periodicity, and the corresponding structures are usually called acoustic or elastic metamaterials. In the following section, we will explain in detail the typical structures, modulating approaches, and existing limitations of both the Bragg scattering and local resonant mechanisms.

Bragg scattering phononic crystals

Typical structures

Periodic structure mediums generating Bragg scattering-type bandgaps can be found both in the solid-state physics area where electron transmission can be controlled [88] and in the electromagnetic domain that presents how photons can be manipulated by photonic crystals [62,89–91]. In all of these structures, periodicity is strictly required. In acoustic domain, the Bragg scattering bandgap phenomenon was first discovered in 1992 in a periodic structure [92], which is composed of scatter inclusions embedded in a homogeneous substrate. Then, the concept of a phononic crystal was first formalized, and a full bandgap calculation was performed [93] for a two-phase periodic composite with cylindrical rods embedded in the matrix. Despite its late starting, the research on phononic crystals or metamaterials has been flourished since 2000 [94]. As previously mentioned, to generate the Bragg scattering bandgap, the lattice constant a should be on the same order as the wavelength λ. Therefore, the larger the geometrical size of the lattice constant is, the lower the bandgap will be. The width and position of the bandgap are also closely related to the contrast of elastic parameters, i.e., the mass density and bulk moduli, between the scatters (ρ, K) and the substrate medium (ρ_0, K_0). As a result, the key point of designing phononic crystals is to manipulate the periodic distribution of the elastic parameters of the scatters and host material. In an empirical manner, scatterers with a low ρ embedded in a substrate with a high ρ_0 tend to provide full bandgap performance, and face-centered cubic (FCC) structures tend to present wider bandgaps than body-centered cube (BCC) structures [95].

One of the most investigated structures of phononic crystals is solid-scatterer-fluid-matrix type, where solid scatterers are embedded in fluid medium, and the shape of the scattered could be cylinder rods [96], a wood-pile [97,98] and so on [99]. Fig. 8 [100–102] shows some typical structures for solid-scatterer-fluid-matrix type phononic crystals. Fig. 8(a) presents a scattering acoustic bandgap found in an artificial sculpture [100] composed of 2D periodic stainless cylinder rods embedded in air. The sculpture shows a Bragg scattering bandgap at approximately 1670 Hz. Fig. 8(b) shows a phononic crystal made of a square lattice of finite cylinders deposited on a homogeneous plate [102]. With the development of manufacturing methods, complex 3D phononic crystals could be easily fabricated, as shown in Fig. 8(c) [101] and Fig. 9 [103,104]. For the 3D soft phononic crystals shown in Fig. 9(b), the bandgap performance could be controlled by applying mechanical deformation [104].

In addition to the periodic solid scatterers embedded in air, their counterparts, i.e., fluid inclusions embedded in solid sub-

Please cite this article in press as: L. Wu et al., Materials Today, (2020), https://doi.org/10.1016/j.mattod.2020.10.006

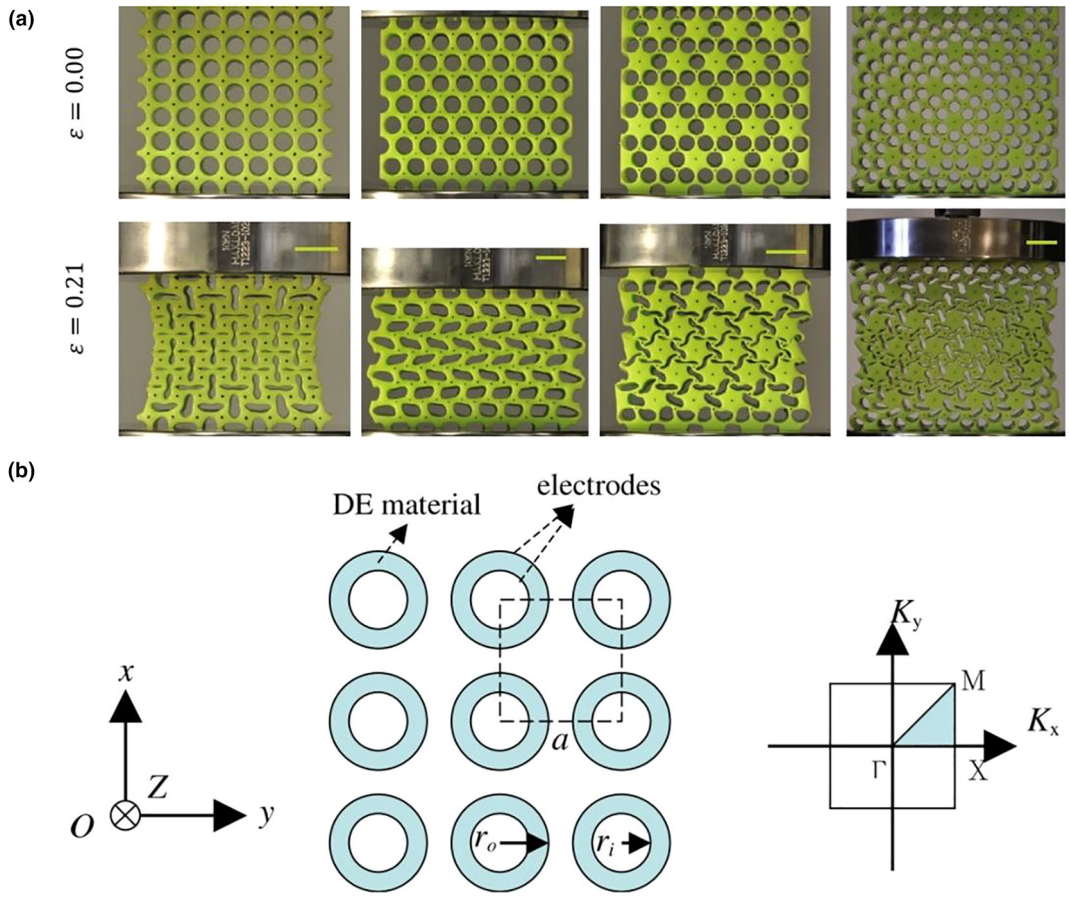

FIGURE 14

(a) Experimental images of four tunable phononic crystals with differently arranged holes loaded under uniaxial compression in the undeformed (top) and deformed (bottom) configuration. (Reprinted with permission from Ref. [119]. 2015, Elsevier.) (b) Two-dimensional cross sections of a phononic crystal composed of square array of hollow dielectric elastomer tubes embedded in air. (Reprinted with permission from Ref. [120]. 1991, IOP Publishing.)

strate [105], could also be adopted to generate bandgaps, as shown in Fig. 10. This type of phononic crystal is easier to integrate with the microfabrication process and therefore presents a relatively high frequency bandgap. For example, by creating microscale periodic cylinder holes on a silicon plate [106] as shown in Fig. 10(a), a complete bandgap from approximately 120 MHz to 150 MHz can be obtained. Fig. 10(b) shows another phononic crystal working in the gigahertz and terahertz frequency ranges when disorders were introduced [107]. Fig. 10(c) shows the first experimental observation [108] of coherent phonon boundary scattering in 2D phononic crystals with minimum characteristic sizes of 4100 nm, while Fig. 10(d) shows a 2D phononic crystal with a bandgap from 600 MHz to 900 MHz [109].

Apart from the solid-scatterer-fluid-matrix and fluid-scatterer-solid-matrix structures, solid-scatterer-solid-matrix phononic crystal is another method to provide wide bandgaps. For example, a phononic crystal composed of W rods periodically distributed in the Si substrate is shown in Fig. 11(a), with a 1.4 GHz center frequency and a wide 800 MHz bandgap [110]. Fig. 11(b) shows a 2D phononic crystal composed of an aluminum alloy plate with periodic holes filled with mercury with a bandgap from 1000 KHz to 1120 KHz [111]. Fig. 11(c) shows the transmission of a Lamb wave in a thin 2D phononic crystal plate made of a periodic gold cylinder embedded in an epoxy substrate [112].

To obtain wider bandgaps, designing periodic hierarchical self-similar elements is an effective approach, as shown in Fig. 12 [113,114]. For example, inspired by natural biocomposites found in shrimp or lobster shells, a hierarchical phononic crystal showing wider bandgaps is presented in Fig. 12(a), and it is found that more bandgaps were opened up than in traditional single-scatterer structures [113]. Other similar structures include Bragg-type "pipes" phononic crystals with a complex hybrid structure [115] and so on [114].

Bandgap tuning methods

The shape of scatterers and their spatial distribution are two crucial factors affecting the bandgaps of phononic crystals. Therefore, by adjusting them, researchers can achieve desired bandgaps. The first tuning method is changing the space distribution of fixed shape scatters. For example, by varying the lattice constant, the bandgap could be modulated, as shown in Fig. 13 (a), which shows periodic cylinder rods embedded in air tuned by origami to suppress traffic noise with an adjustable frequency range from 500 Hz to 1200 Hz [116]. Specifically, if the unit cell of the phononic crystal is not cylindrically symmetric (such as a

Please cite this article in press as: L. Wu et al., Materials Today, (2020), https://doi.org/10.1016/j.mattod.2020.10.006

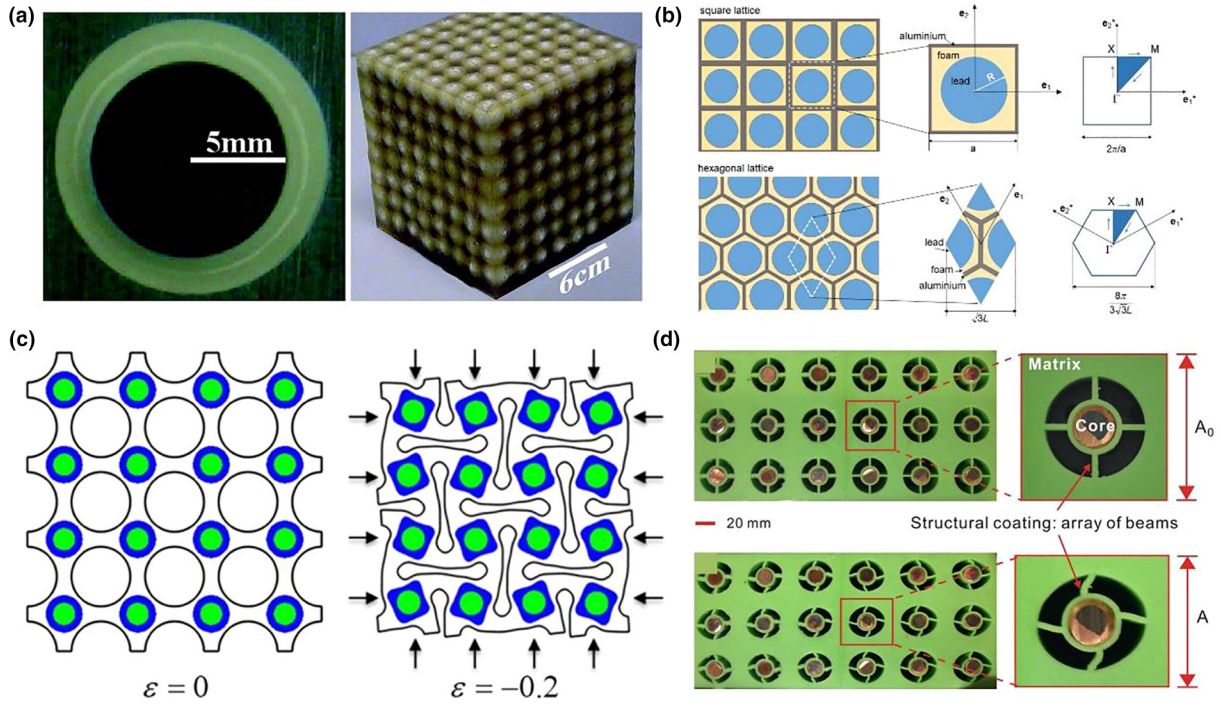

FIGURE 15

(a) Cross section of a coated lead sphere (left) that forms the basic structure unit for an 8 × 8 × 8 sonic crystal (right). (Reprinted with permission from Ref. [123]. 2000, The American Association for the Advancement of Science.) (b) Sketch of two locally resonant acoustic metamaterials composed by aluminum cells of square (Top) and hexagonal (Bottom) shape, filled by a soft material with a heavy circular inclusion. (Reprinted from Ref. [124]) (c) Acoustic metamaterials comprising elastomeric matrix with a square array of circular holes and resonating elements (including elastomeric coating (blue) and resonating mass (green)), whose geometry can be reorganized by instability subjected to equibiaxial compression. (Reprinted with permission from Ref. [125]. 2020, Elsevier.) (d) Top: The undeformed configuration comprises resonating units dispersed into an elastomeric matrix, where each resonator consists of a metallic mass connected to the matrix through elastic beams. Bottom: When a compressive strain is applied in the vertical direction, buckling of the beams significantly alters the effective stiffness of the structural coating, which in turn changes the band gap frequency. (Reprinted with permission from Ref. [16]. 2014, American Physical Society.)

hexagonal, square or triangular shape), then gradually rotating the scatterers embedded periodically in air has proven to be an effective way to achieve adjustable bandgaps [117], as shown in Fig. 13(b), without refabricating another phononic crystal with a different size [118].

Although not as efficient as tuning the lattice constant, deforming the shape of scatters by applying an external force is an alternative approach for obtaining tunable bandgaps of phononic crystals. For example, by compression or stretching soft phononic crystals, researchers can adjust the bandgap of soft phononic crystals embedded by various porous holes [119], as shown in Fig. 14(a). Fig. 14(b) shows a 2D phononic crystal composed of hollow dielectric elastomer cylinders [120], which are sandwiched between two compliant electrodes. By applying a voltage between the compliant electrodes, the elastic bandgaps are changed due to the radial strain of the dielectric elastomer. Other tuning methods for Bragg scattering-type bandgaps include applying a periodic external potential [121] to phononic crystals, changing the filling fractions of scatterers [122] and so on.

Local resonance mechanism

To break the geometrical size limitation of phononic crystals based on the Bragg scattering mechanism, researchers have consistently looked for approaches to achieve a lower frequency bandgap with smaller sized unit cells. A local resonance mechanism emerged as desired, which was first proposed by Liu's group in 2000 [123], as shown in Fig. 15 [16,123–125]. Elastic energy with specific frequency could be constrained by resonators [125]. Unlike Bragg scattering-type bandgaps, which require a lattice constant comparable to the wavelength λ ($\lambda \approx a$), this composite material is shown to exhibit bandgaps with a feature size a that is orders of magnitude smaller than λ. From the first local resonant sonic crystals, an increasing number of acoustic metamaterials have been investigated based on the local resonant idea [126–131]. These materials could be applied to absorb impact energy [132], vibration suppression [133] and simultaneous vibration suppression and energy harvesting functions [51]. The external vibration energy could be trapped and transferred into the kinetic energy of the resonators and then further converted into electric energy through the mechano-electrical conversion of its integrated piezoelectric elements. Unlike the Bragg scattering-type phononic crystals, locally resonant metamaterials do not require a periodicity of elements, and resonators could be distributed throughout the matrix material randomly [123,134]. Although, however, local resonators are usually arranged in a periodical configuration in the metamaterials.

Please cite this article in press as: L. Wu et al., Materials Today, (2020), https://doi.org/10.1016/j.mattod.2020.10.006

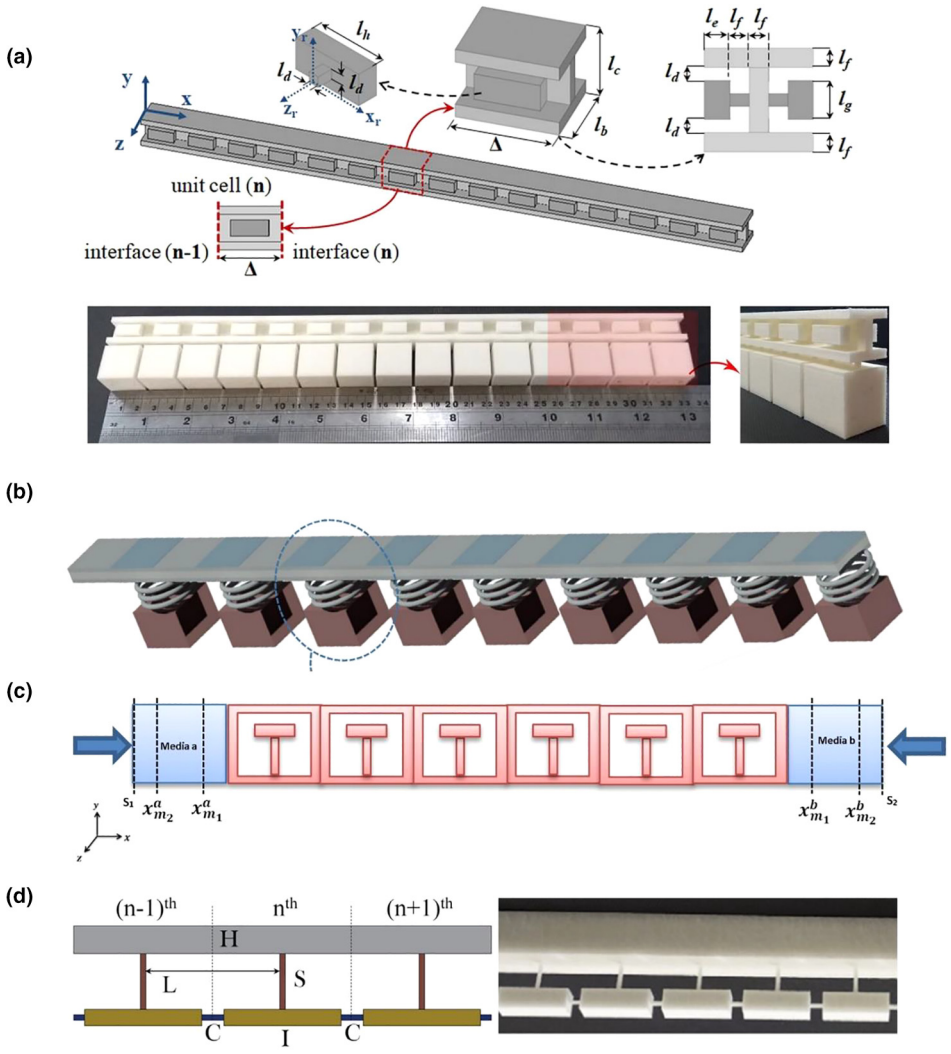

FIGURE 16

(a) Top: 3D view of the cantilever-in-mass metamaterial beam and its unit cell with the nominal geometric dimensions. Bottom: Metamaterial beam with attached cube specimens constructed by 3D printing. (Reprinted with permission from Ref. [137]. 2019, Springer Nature.) (b) Schematic of the combined mechanical-electromechanical metastructure. (Reprinted with permission from Ref. [138]. 2018, Elsevier.) (c) Schematic of a finite array of 6 T-shape resonant unit cells. (Reprinted with permission from Ref. [139]. 2019, Elsevier.) (d) Left: 1D metamaterial beam model: host structure H (in gray color), inertia-like elements I (in yellow color), spring-like elements S (in red color) and interconnections C (in blue color). Right: Fabricated metamaterial beam sample with interconnected resonators. (Reprinted with permission from Ref. [140]. 2018, Elsevier.)

Typical resonator structures

Fig. 15(b) presents cellular locally resonant metamaterials constituted by a cellular metallic lattice filled by a soft light material with heavy inclusions or resonators [124]. Similar structures include elastic rubber-coated mass inclusions distributed within the chiral circular ring nodes of unit cells [135]. Under compression, the deformation-induced geometry and material nonlinearities of the soft matrix and coating could be utilized to tune the dynamic responses of acoustic metamaterials, as shown in Fig. 15(c) [125]. The soft coating of acoustic resonators could also be replaced by other elastic components, such as a metallic core connected to the substrate through elastic beams, whose buckling is adopted to control the propagation of elastic waves, as shown in Fig. 15(d) [16,136].

Spring-mass resonant acoustic beams are shown in Fig. 16 [137–140], where Fig. 16(a) shows a spatially variant locally resonant bandgap that progressively slows down the group velocity until an almost zero value, leading to an energy trapping effect near the lower bandgap boundary [137]. Fig. 16(b) presents a metamaterial cantilever with hybrid mechanical and electromechanical resonators to achieve a wider bandgap [138]. Fig. 16(c) shows a periodic microstructure at a small length scale and low-frequency bandgaps by the introduction of a resonant inclusion [139]. Fig. 16(d) describes beam and plate metamaterials with interconnected local resonators to form a hybrid resonant mode [140].

It was found that damping can sometimes broaden the bandgap through the analysis of wave transmission [72]. A mass-in-mass dissipative resonator is shown in Fig. 17(a), which presents an elastic metamaterial with multiple dissipative resonators [141] for broadband wave mitigation. Fig. 17(b) shows dissipative acoustic metamaterials with various types of damped oscillator

Please cite this article in press as: L. Wu et al., Materials Today, (2020), https://doi.org/10.1016/j.mattod.2020.10.006

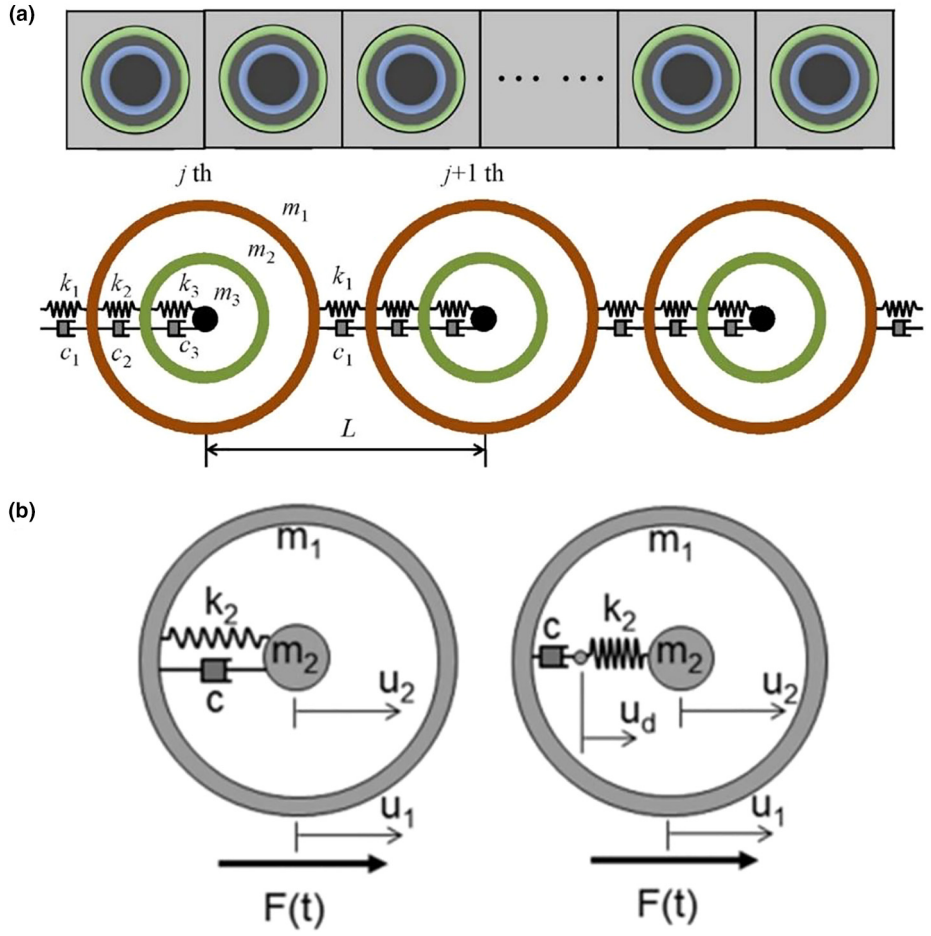

FIGURE 17

(a) Top: Schematic design of a dissipative elastic metamaterial. Bottom: a dissipative mass-in-mass lattice system with two resonators. (Reprinted with permission from Ref. [141]. 2016, Elsevier.) (b) Left: Locally dissipative microstructure with a Kelvin-Voigt-type oscillator. Right: Locally dissipative microstructure with a Maxwell-type oscillator. (Reprinted with permission from Ref. [71]. 2014, AIP Publishing.)

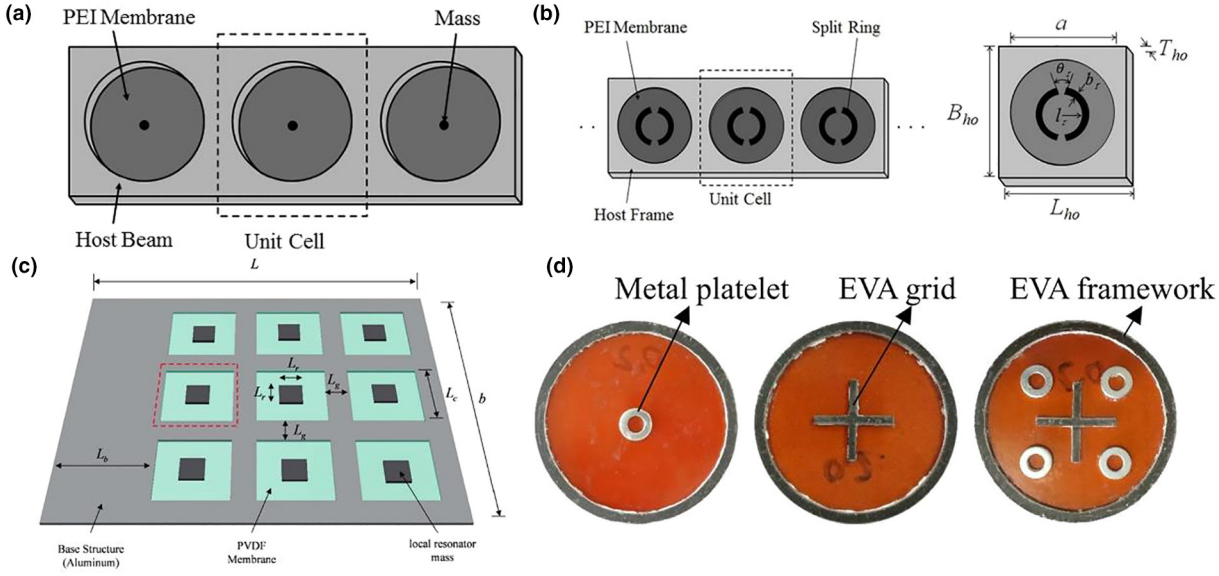

FIGURE 18

(a) A metamaterial beam with circular membrane-mass structures. (Reprinted from Ref. [142]) (b) A metamaterial beam with membrane-split-ring resonators. (Reprinted with permission from Ref. [143]. 2019, SAGE Publications.) (c) A metamaterial plate with periodic local resonances. (Reprinted with permission from Ref. [144]. 2016, SAGE Publications.) (d) Membrane-type acoustic metamaterial samples with different resonator structures. (Reprinted with permission from Ref. [145]. 2020, Elsevier.)

Please cite this article in press as: L. Wu et al., Materials Today, (2020), https://doi.org/10.1016/j.mattod.2020.10.006

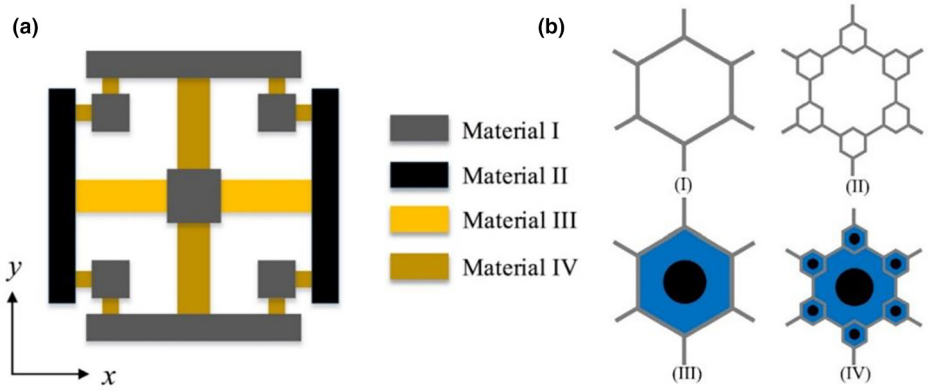

FIGURE 19

(a) A 2D anisotropic elastic metamaterial unit cell exhibiting multiple local resonances. (Reprinted from Ref. [146]) (b) Top: regular honeycomb (left) and first order hierarchical honeycomb (right). Bottom: Regular honeycomb with embedded resonators (left) and first order hierarchical honeycomb with embedded resonators (right). (Reprinted with permission from Ref. [147]. 2019, Elsevier.)

microstructures presenting stress wave attenuation performance [71].

Compared with core–shell, mass-in-mass, and cantilever type resonators, mass-in-membrane resonators are easier to fabricate, flexible and lightweight. Typical structures are shown in Fig. 18 [142–145]. Fig. 18(a) shows a metamaterial beam with circular membrane-mass structures [142]. By introducing energy harvesting devices, membrane-type metamaterials can simultaneously attenuate waves and harvest energy, as shown in Fig. 18(b) [143]. Similar structures include a metamaterial composed of periodic locally resonant membranes arranged in a square array [144] and a low-frequency membrane-type acoustic metamaterial [145] with wide sound attenuation frequency.

Like Bragg scattering phononic crystals, the utilization of self-similar hierarchical resonant structures could broaden the band-gap of acoustic/elastic metamaterials because of the existence of

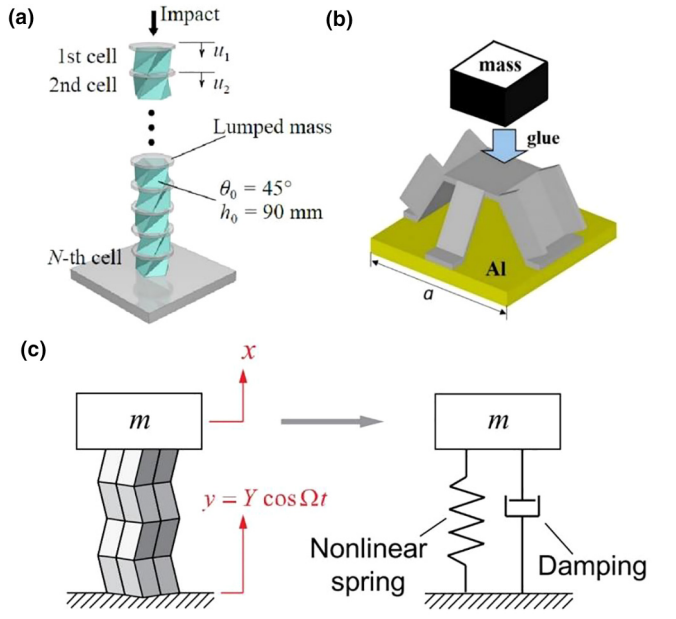

FIGURE 20

(a) Illustration of a homogeneous chain of the triangulated cylindrical origami. All of the unit cells are identical. (Reprinted from Ref. [156]) (b) Design of a kirigami-based elastic metamaterial by attaching the kirigami cell on a bottom plate with glued mass block. (Reprinted with permission from Ref. [157]. 2018, Springer Nature.) (c) Left: Schematic diagram of using fluidic origami for base vibration isolation. Right: An equivalent system. (Reprinted with permission from Ref. [149]. 2018, American Society of Mechanical Engineers.)

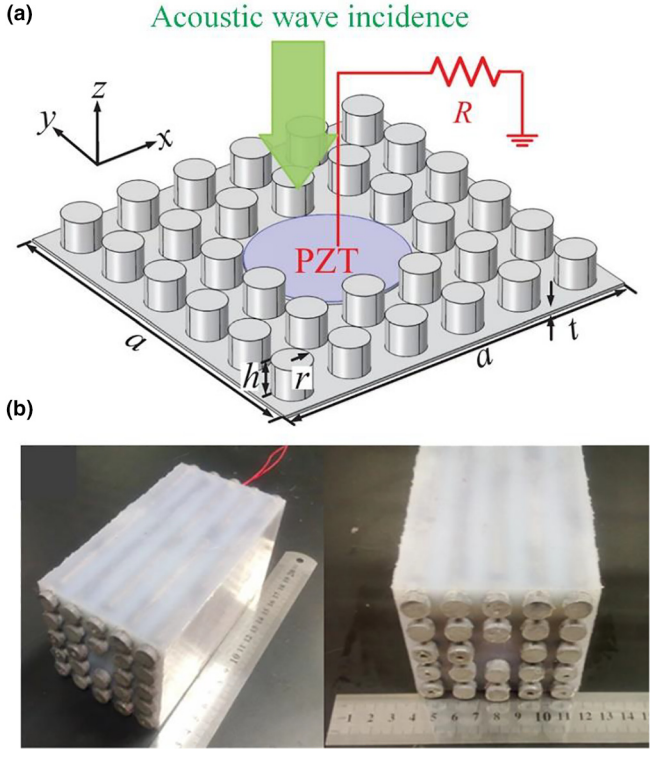

FIGURE 21

(a) Sketch of an acoustic energy harvesting system composed of a defected supercell with a piezoelectric patch and a load circuit. (Reprinted with permission from Ref. [75]. 2016, AIP Publishing.) (b) A phononic crystal for vibration energy harvesting with a PVDF film in the middle of the defect. (Reprinted with permission from Ref. [158]. 2013, AIP Publishing.)

Please cite this article in press as: L. Wu et al., Materials Today, (2020), https://doi.org/10.1016/j.mattod.2020.10.006

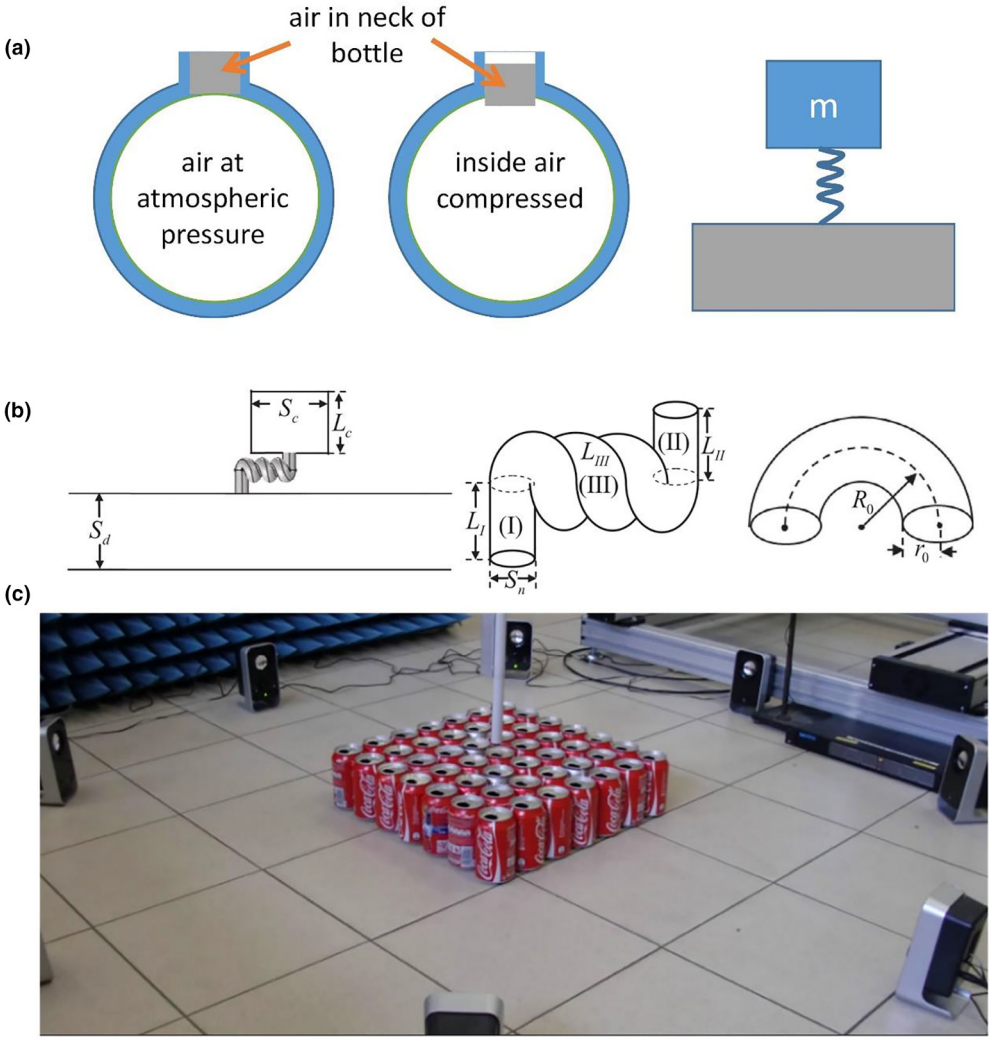

FIGURE 22

(a) Schematic of a HR structure (left) and its equivalent system (right). (b) A Helmholtz resonator with a spiral neck with three turns. (Reprinted with permission from Ref. [172]. 2017, Elsevier.) (c) A periodic ensemble of 7 × 7 soda cans acting as Helmholtz resonators. (Reprinted with permission from Ref. [173]. 2011, American Physical Society.)

multiple resonance [74]. Typical examples are shown in Fig. 19 [146–148], where Fig. 19(a) shows an anisotropic elastic metamaterial [146] consisting of a series of properly arranged periodic elements. The hierarchical element enables the model with broad bandgaps in the low frequency range. Fig. 19(b) shows a metamaterial with a honeycomb hierarchical lattice with embedded rubber-coated lead cylinders, which possess the ability to efficiently filter waves at various frequencies [147].

Origami/kirigami structures [149–155] could also be utilized as lightweight local resonators to generate bandgaps, as shown in Fig. 20 [149,156,157], which shows the formation of frequency band structures composed of the triangulated cylindrical origami [156]. Fig. 20(b) shows a kirigami elastic metamaterial with anisotropic mass density to manipulate flexural waves [157], which was constructed by attaching the resonant kirigami structures periodically on the top of a host plate. Fig. 20(c) shows a pressurized fluidic origami cellular solid for low-frequency base excitation isolation, which is derived from the nonlinear geometric relations between folding and internal volume change [149].

By removing one or several elements in the periodic structures, a resonant cavity will be formed, which could be easily integrated with energy harvesting functions, as shown in Fig. 21 [175,158]. Fig. 21(a) is an acoustic energy harvester [75] based on a defective acoustic metamaterial with piezoelectric material by creating resonant defects to confine the strain energy from an acoustic incidence. Similar ideas include a vibration energy harvesting generator using a point-defect phononic crystal with a piezoelectric material [158], as shown in Fig. 21(b). By removing a rod from a perfect phononic crystal, the waves with resonant frequency were localized and enhanced in the resonant cavity.

The Helmholtz resonator (HR) [159–171] is also a fundamental acoustic device and is generally used to reduce low-frequency noise, as shown in Fig. 22(a). However, this resonator is only effective at its single resonance peak with a narrow frequency

Please cite this article in press as: L. Wu et al., Materials Today, (2020), https://doi.org/10.1016/j.mattod.2020.10.006

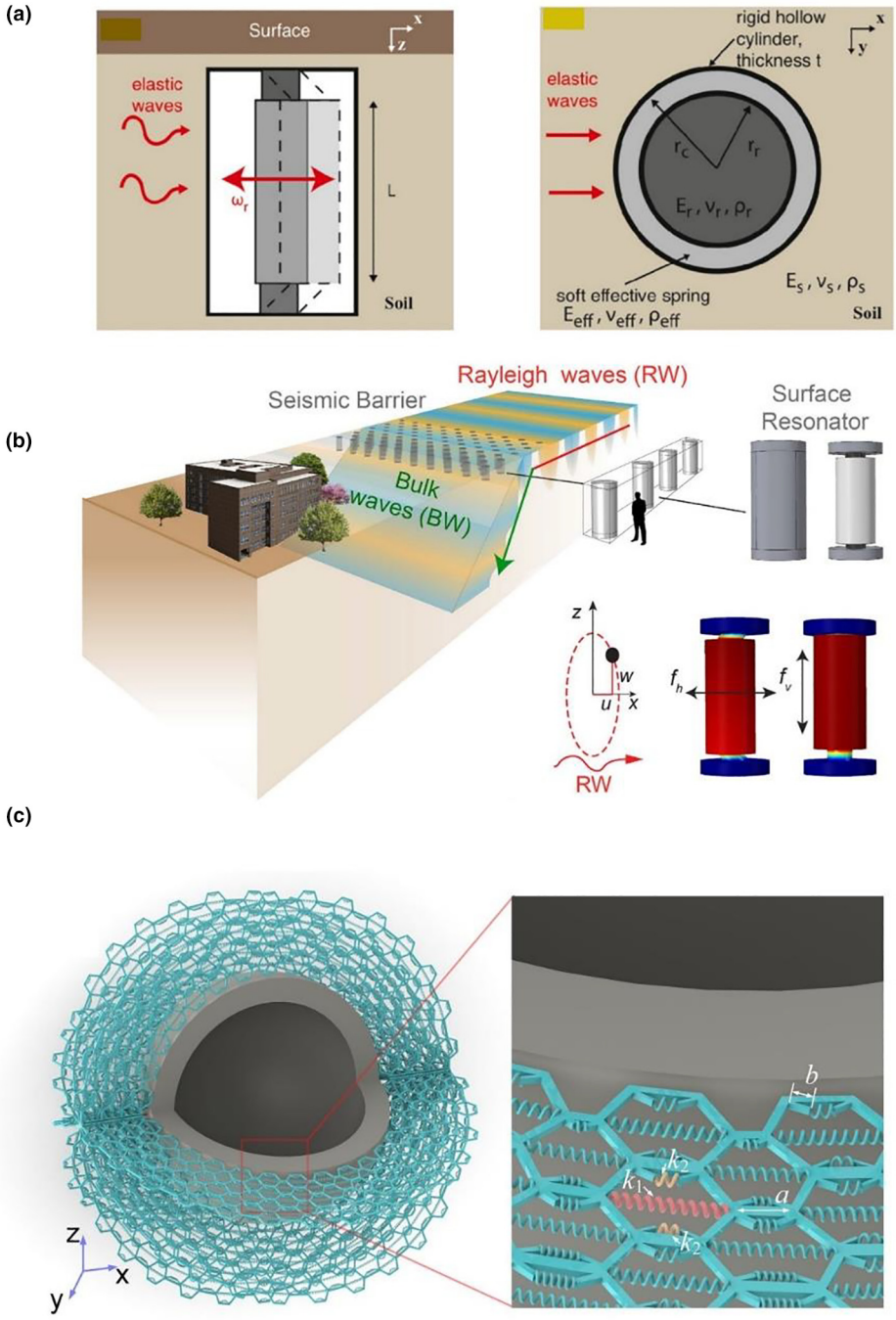

FIGURE 23

(a) Left: Illustration of a resonator, which is a cylindrical hollow tube containing a heavy bulk cylinder suspended by polymeric springs (black). Right: The two-dimensional representation of the system. (Reprinted with permission from Ref. [175]. 2015, Elsevier.) (b) Seismic barrier of a series of acoustic resonators. (Reprinted with permission from Ref. [176]. 2016, Springer Nature.) (c) Illustration of a mechanical metamaterials as a shell to shield the object in the core from the input energy flow. (Reprinted with permission from Ref. [13]. 2020, Elsevier.)

bandwidth. Some HRs are shown in Fig. 22(b) and (c) [172,173]. An extended neck or a spiral neck shown in Fig. 22(b) replaces the traditional straight neck of the HR to improve the noise attenuation performance [172] at low frequencies with a limited space. Fig. 22(c) proves that broadband sounds can be controlled and focused at will on a subwavelength [173] scale by soda can HRs.

Local resonant tuning methods

The key parameters for a local resonator to react with acoustic/elastic waves are the effective mass component M and the effective stiffness K. Therefore, the tuning methods can be divided into two types. The first is to adjust the effective mass component of the resonator, and the second is to control the stiffness part of the resonator. The effective dynamic properties of the

Please cite this article in press as: L. Wu et al., Materials Today, (2020), https://doi.org/10.1016/j.mattod.2020.10.006

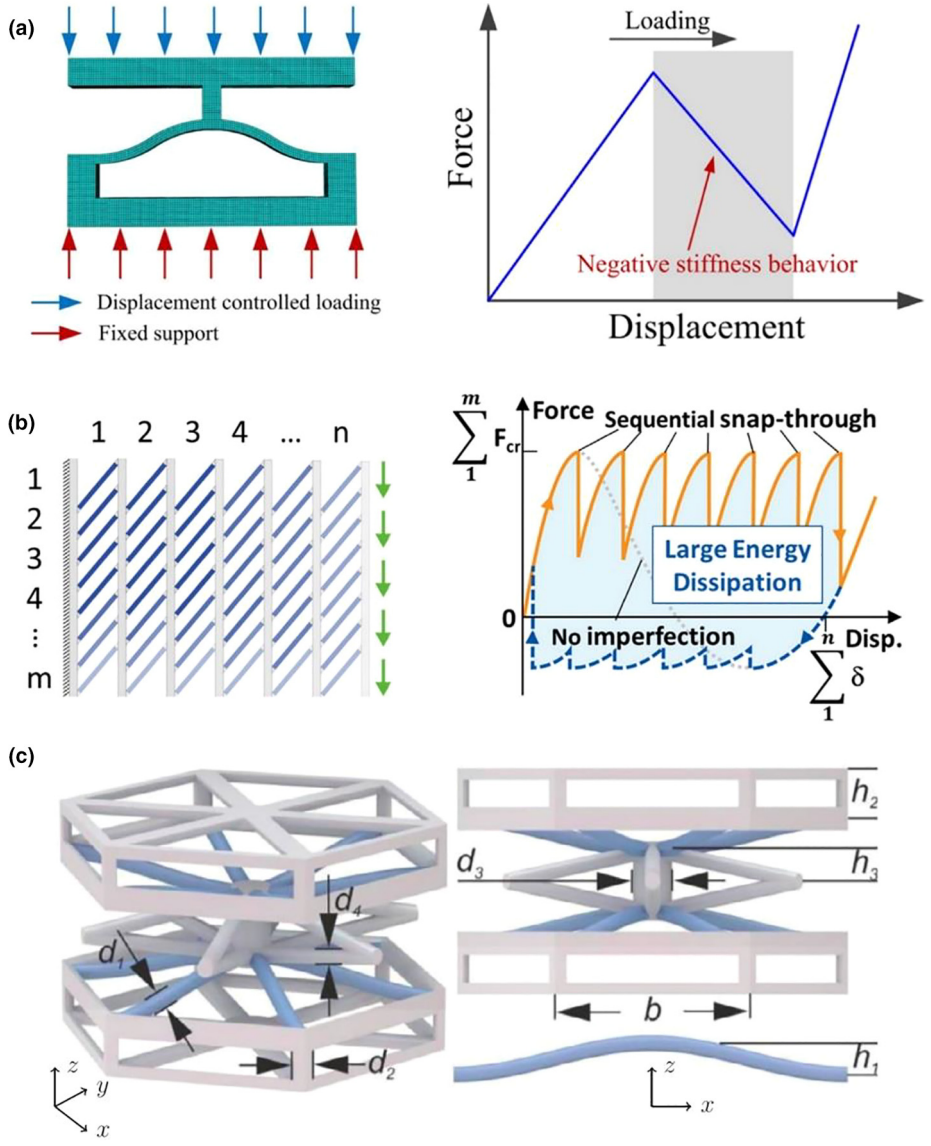

FIGURE 24

(a) Left: A curved beam structure used to achieve negative stiffness behavior. Right: Force-displacement curve of negative stiffness element. (Reprinted with permission from Ref. [189]. 2019, Elsevier.) (b) An array of m×n connected units (left) and its sequential snap-through response curve under an applied displacement with energy dissipation (right). (Reprinted with permission from Ref. [190]. 2019, Elsevier.) (c) Unit cell of a hexagonal frame and connection elements (grey) between a parallel buckling element (blue). (Reprinted with permission from Ref. [192]. 2017, Elsevier.)

locally-resonant metamaterials can be calculated numerically [174].

To lower the bandgap region, increasing the mass could be an efficient method. For example, large resonators could be utilized to obtain an extremely low frequency band, as shown in Fig. 22 (a) and (b) [175,176]. Each resonator consists of a mass component suspended by soft bearings that prevents the propagation of seismic waves with frequencies below 10 Hz and is suitable for the protection of large buildings [175,177]. However, this method would lead to a bulky and heavy resonator, which is undesired in practical applications. To solve this problem, inertial amplification is an important method for achieving wide bandgaps at low frequencies without adding additional resonating components [178–180]. By employing inertial amplification, the effective mass of a small component could be amplified by using displacement amplification mechanisms [181].

Compared with dealing with the mass component, controlling the effective stiffness is more feasible. As is known, the lower the effective stiffness is, the lower the resonant frequency of the local resonator is, and the lower the bandgap of the acoustic/elastic metamaterials is. Based on this idea, various quasi-zero-stiffness metamaterial [182–184] have been designed to suppress mechanical vibrations in the low frequency range. Specifically, an absolute zero-stiffness resonator could theoretically lead to a bandgap from 0 Hz to infinity, as shown in Fig. 22(c) [13], which shows a mechanical metamaterial for perfect energy shielding in the full frequency band [13]. Some mechanical resonators with local resonators could exhibit an unusual frequency-dependent

Please cite this article in press as: L. Wu et al., Materials Today, (2020), https://doi.org/10.1016/j.mattod.2020.10.006

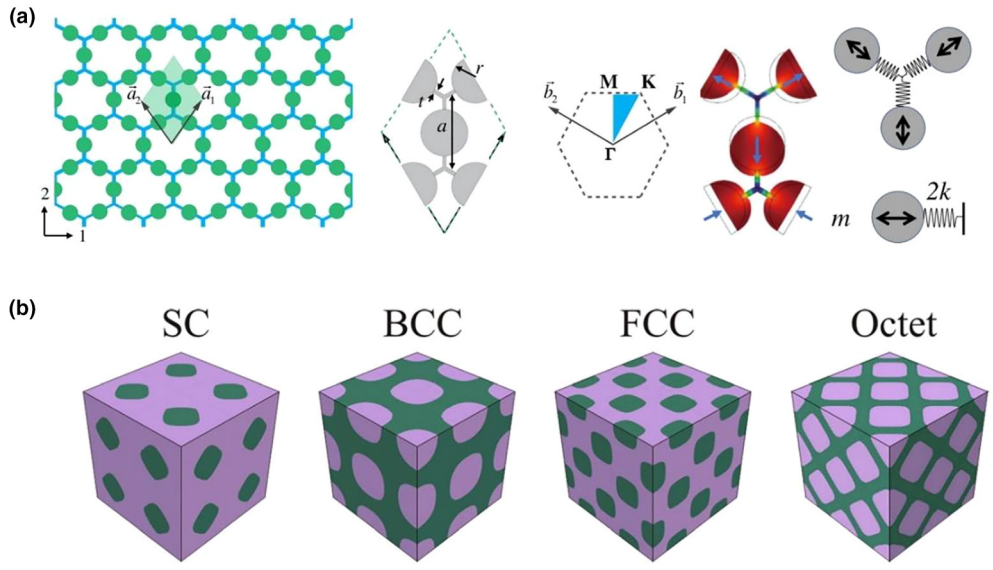

FIGURE 25

(a) The geometry of the 2D phononic crystal with concentrated masses at the middle of each hexagonal edge (left). The unit cell is marked by the shaded region and its ninth Bloch mode is shown in the right part of the picture. (Reprinted with permission from Ref. [202]. 2018, American Physical Society.) (b) Triply periodic co-continuous acoustic metamaterials consisting of 2 × 2 × 2 unit cells with simple cubic lattice (SC), body-centered cubic lattice (BCC), face-centered cubic lattice (FCC), and octettruss lattice (Octet). (Reprinted with permission from Ref. [204]. 2014, AIP Publishing.)

effective stiffness that can become unbounded or extremely small at specific frequencies, resulting in a largely tunable bandgap [185].

For shock absorption and dissipation, multistable structures based on negative stiffness caused by sequential snap-through instabilities [186–188] could be adopted. It is demonstrated that by precisely designing the architecture of a lattice structure, it is possible to create lightweight and strong structures that are highly energy absorbing and able to recover their shape after deformation. Typical 2D and 3D multistable mechanical metamaterials for energy absorption are shown in Fig. 24 [189–192], where the mechanical energy could be stored or dissipated by the deformed beams. Fig. 24(a) shows a structure dissipating energy through deformation and exhibits negative stiffness behavior through inelastic instability [189], while Fig. 24(b) shows a metamaterial for tailorable shear behavior and energy dissipation [190].

Coupling local resonance and Bragg scattering

Although acoustic/elastic metamaterials could achieve low-frequency bandgaps by using subwavelength resonators, their bandgaps are usually narrow, which brings limitations in the application where broadband vibrations or sound are expected to be suppressed. Usually, when periodic local resonators are utilized, it shows the coupling effects of the local resonances and Bragg scattering [193–197]. Therefore, by combining the bandgap formation mechanisms of Bragg scattering and local resonances [198–201], wide and low phononic bandgaps can be established [202,203], as shown in Fig. 25(a). Fig. 25(b) shows a group of metamaterials exhibiting a broadband wave filtering capability [204], which is attributed to the coupling effects of the local resonances and Bragg scattering.

In seismic wave protection areas, both Bragg scattering and local resonant bandgaps usually exist in mechanical metamaterials, which open up new routes in civil building protection [205], as shown in Fig. 23(a) and (b), as previously mentioned [175,176], where an array of resonating structures were buried around sensitive buildings.

Other examples that demonstrate a coupling of the local resonance and the Bragg scattering effect [199] are shown in Fig. 26. The combined characteristics of the periodic and locally resonant features in metamaterial structures [200] shown in Fig. 26(b) give rise to relatively low and wide bandgaps. In addition, the bandgap of the metamaterial could be thermally tuned through changes in temperature. The element is composed of materials with different moduli, which have drastically different temperature dependences, to preferentially tune the modulus of the lattice material compared to the resonant inclusion. Fig. 26 (c) shows the enlargement of the locally resonant acoustic bandgap [201] in 2D sonic crystals with double-sided stubbed plates, which is due to the coupling between the resonant eigenmodes of the periodic stubs located on each plate side.

Physical mechanisms to intervene in the direction of the energy flow

Waveguide by defects

Phononic crystals with line defects [206] could be applied to control the direction of the energy flow. By introducing localized defects (cavities, wave guides, stubs, etc.) inside periodic structures, a resonating cavity can be constructed [207]. Acoustic or elastic wave energy is highly confined [64] in the defect area, which leads to the manipulation of the sound or elastic wave propagation direction [11,102,208–209]. Typical structures with defects to guide acoustic or elastic wave propagation are shown in Fig. 27 [11,210–212]. Fig. 27(a) presents a waveguide formed

Please cite this article in press as: L. Wu et al., Materials Today, (2020), https://doi.org/10.1016/j.mattod.2020.10.006

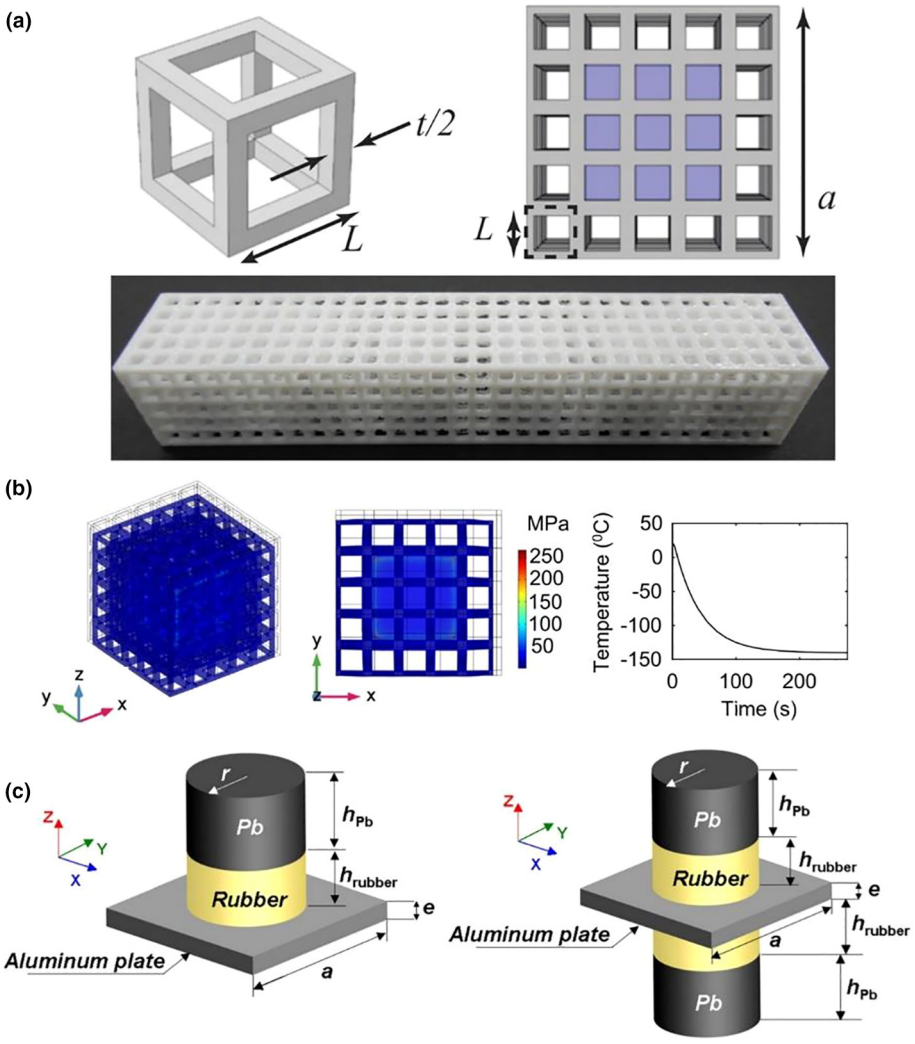

FIGURE 26

(a) Top: Metastructure composed of mesoscale unit cell (right) with a lattice embedded resonator (area in purple). Bottom: Final 3D-printed metastructure with embedded resonators. (Reprinted from Ref. [199]) (b) Thermally tune the band gaps of metamaterials, which combine a periodic lattice and locally resonant inclusions by applying a temperature change and allow the meta-structure unit cell to expand or contract. (Reprinted with permission from Ref. [200]. 2019, Elsevier.) (c) Left: A unit cell of one-side stubbed plate with composite stub. Right: Double-side stubbed plate with composite stub. (Reprinted with permission from Ref. [201]. 2012, AIP Publishing.)

by a chain of cavities created by the selective fluid filling of holes in a solid phononic crystal. The filled holes become cavities that sustain acoustoelastic defect modes [210]. As a result, an arbitrary phononic circuit can be created that can be applied as various bending waveguides or wave splitters. Fig. 27(b) shows the realization of a tunable valley phononic crystal composed of hybrid channel-cavity cells with tunable parameters [211], and multiple functions including splitting waves, guiding waves at different frequencies along distinct paths, and steering waves through positive/negative refraction. Fig. 27(c) shows two models that can be used to realize the directional transmission effect [212]. Defects could also be adjusted by adjusting the inner radius of the hollow cylinders and the transmission of waves at different frequencies can be achieved [213]. Fig. 27(d) shows a coupled-resonator elastic waveguides formed by a chain of cavities in a two-dimensional phononic crystal slab with cross holes. The authors realized a straight waveguide and a wave splitting circuit with 90° bends.

Programming wave trajectory by transformation acoustics

Transformation acoustics [40,69], as an analog of transformation optics, was first introduced by Cummer and Schurig [47]. This method was performed based on the invariance of the acoustic wave equation under coordinate transformations [38]. By applying transformation acoustics, researchers could draw on the relationship among the coordinate transformation and material properties and design microsuperlens [214] for acoustic waves. When the material distribution in the physical system (ρ_{eff}, K_{eff}) is properly designed, it is possible to find a coordinate transformation $r \rightarrow r'$ (suppose $r = x_1 i_1 + x_2 i_2 + x_3 i_3$ is described with the Cartesian coordinate, and $r' = q_1 j_1 + q_2 j_2 + q_3 j_3$, where j_1, j_2 and j_3 are respective unit vectors), which makes the corresponding acoustic field take the form in the new coordinate system, without breaking the form of the wave equation. However, the ideal material parameters prescribed by this methodology are complex and challenging to obtain experimentally and are usu-

Please cite this article in press as: L. Wu et al., Materials Today, (2020), https://doi.org/10.1016/j.mattod.2020.10.006

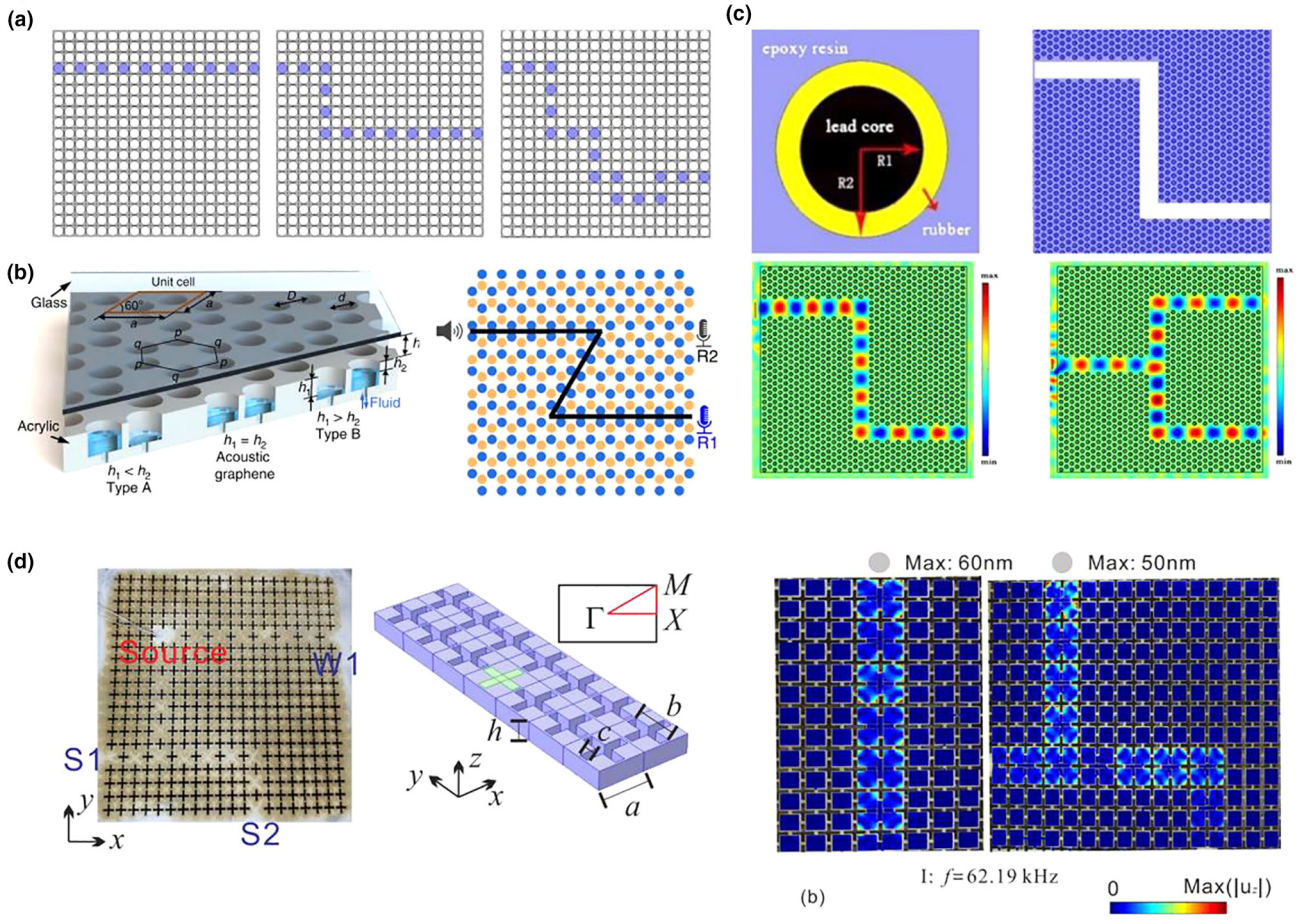

FIGURE 27

(a) Cross sections of coupled-resonator acoustoelastic waveguides formed by filling holes with water in different circuits on a finite phononic crystal with 19 × 19 cells. Left: Straight waveguide. Middle: Two-bend waveguide. Right: Eight-bend waveguide. (Reprinted with permission from Ref. [210]. 2017, American Physical Society.) (b) Left: Schematic of the phononic crystals composed of a glass ceiling and an acrylic plate with cylindrical cavities distributed in honeycomb lattices. Right: Valley phononic crystals with configurations for a transporting acoustic wave along a Z-shaped path. (Reprinted with permission from Ref. [211]. 2020, Springer Nature.) (c) Top: A resonant unit cell (left) and an acoustic channel structure with line defect as a waveguide (right). Bottom: Distribution of acoustic field in directional transmission model of a continuous channel (left) and a bifurcated channel (right). (Reprinted with permission from Ref. [212]. 2019, AIP Publishing.) (d) Left: A coupled resonator elastic waveguides. Right: field distributions of displacement measured at 62.19 KHz for the straight waveguide and the wave splitter, respectively. (Reprinted with permission from Ref. [11]. 2018, Elsevier.)

ally highly anisotropic and inhomogeneous. Fortunately, composite materials with embedded subwavelength resonators can exhibit nearly arbitrary values of effective density and modulus tensors to satisfy the demanding material requirements in transformation acoustics. Inspired by electromagnetic waveguide cloaks [215] with GRIN metamaterials, similar structures are designed to accomplish the requirements of acoustic cloaking [40] by acoustic metamaterials, whose elastic parameters could be properly mapped in order to satisfy the acoustic properties under request. Fig. 28(a) shows an acoustic cloak design process [42], such that sound incident from all directions passes through and around the cloak as though the object does not exist. The undeformed region Ω is transformed by the mapping X into the cloak space ω. A single point O is transformed into a hole, which is the invisible region and is surrounded by the cloak ω. The outer boundary $\partial\omega+$ is coincident with $\partial\Omega+(=\partial\Omega)$, and the inner boundary $\partial\omega-$ is the image of the singular point O. The first practical realization of a cylindrical cloak for linear surface liquid waves [44] could effectively bend surface waves radiated by a closely located acoustic source. Since then, various acoustic cloaks have been created based on the acoustic transformation approach for homogeneous [35,49] or inhomogeneous background media [20]. Fig. 28(b) shows an acoustic cloak being divided into any number of arbitrary triangular patterns [18], which are mapped from similar patterns in virtual space. The cloak could transform one triangular domain to various other shapes. The resulting cloak is composed of homogeneous triangular parts, each having just two alternating layers of the material.

GRIN [216–219] materials are essentially important for achieving the distribution mapping of elastic parameters by transformation acoustics and demonstrate broad applications in wave focusing [220] wave guiding [207], beam width modulating [221], directional beam steering [222,223], mirage [224], energy harvesting [56,225] and so on [226]. These materials are often realized by the gradual modification of the filling fraction [220,227,228], the size of the units [229], the lattice constant, the material parameters and so on [230].

Please cite this article in press as: L. Wu et al., Materials Today, (2020), https://doi.org/10.1016/j.mattod.2020.10.006

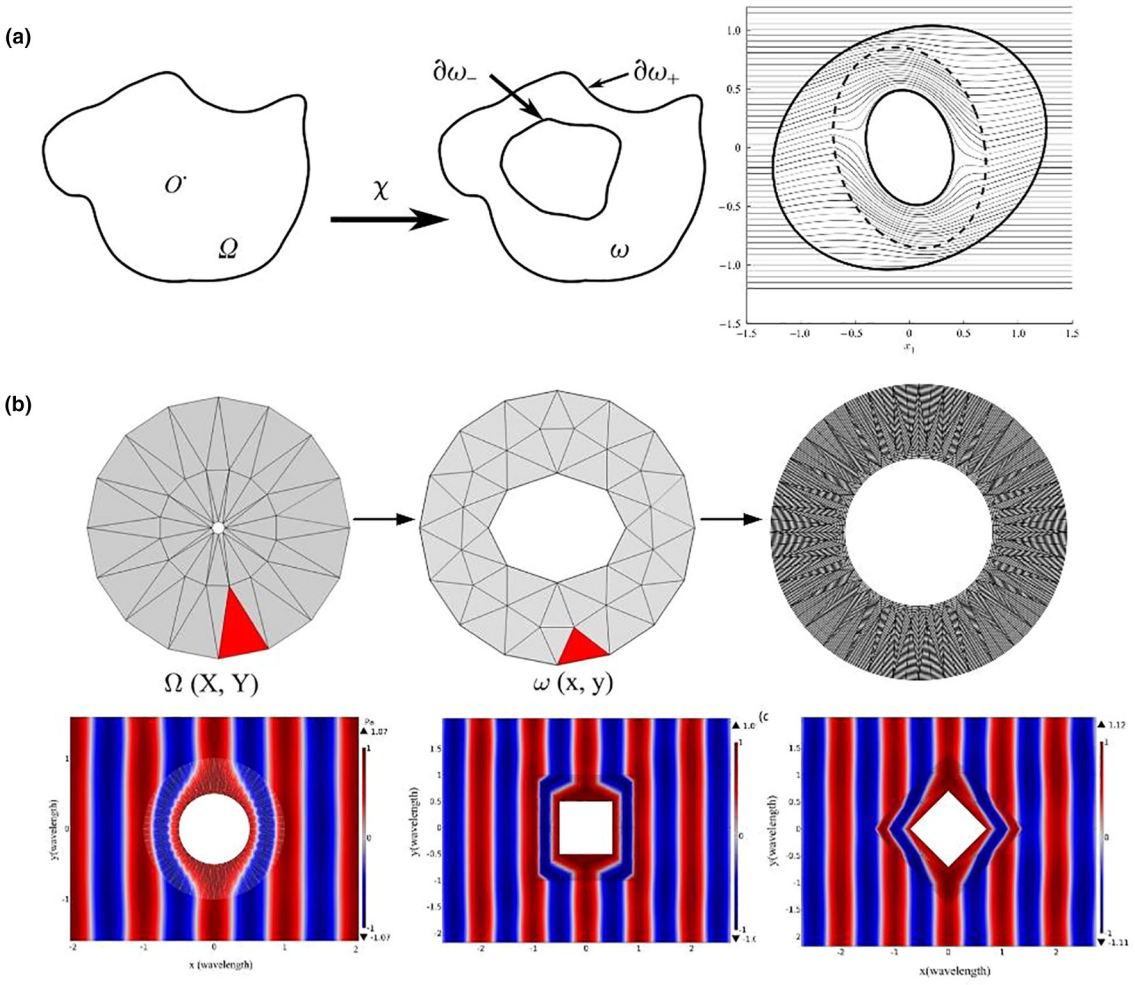

FIGURE 28

(a) The undeformed simply connected region Ω is transformed by the mapping χ into the multiply connected cloak ω. (Reprinted with permission from Ref. [42]. 2008, The Royal Society (U.K.).) (b) Top: Transformation from virtual space (left) to physical space (middle) with similar patterns and an approximate circular cloak with sections of three homogeneous parts built with layered structures (right). Bottom: The pressure field for a plane wave with amplitude of 1Pa with circular cloak (left), square cloak direction 1 (middle) and square cloak, direction 2 (right). (Reprinted from Ref. [18]).

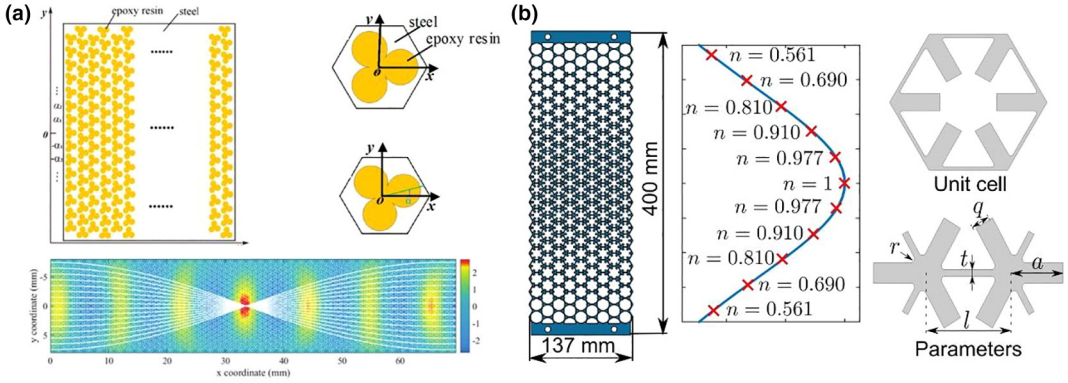

FIGURE 29

(a) Left: A schematic graph of GRIN phononic crystal lens with a rotating scatterer, Right: The original position of the lattice (top) and the scatterer with a rotation angle of α (bottom). (Reprinted from Ref. [231]) (b) Pentamode lens design. Left: The top view of the designed lens. Middle: The discretized index distribution within the lens. Right: The unit cell structure and parameters. (Reprinted with permission from Ref. [232]. 2017, Acoustical Society of America.)

Please cite this article in press as: L. Wu et al., Materials Today, (2020), https://doi.org/10.1016/j.mattod.2020.10.006

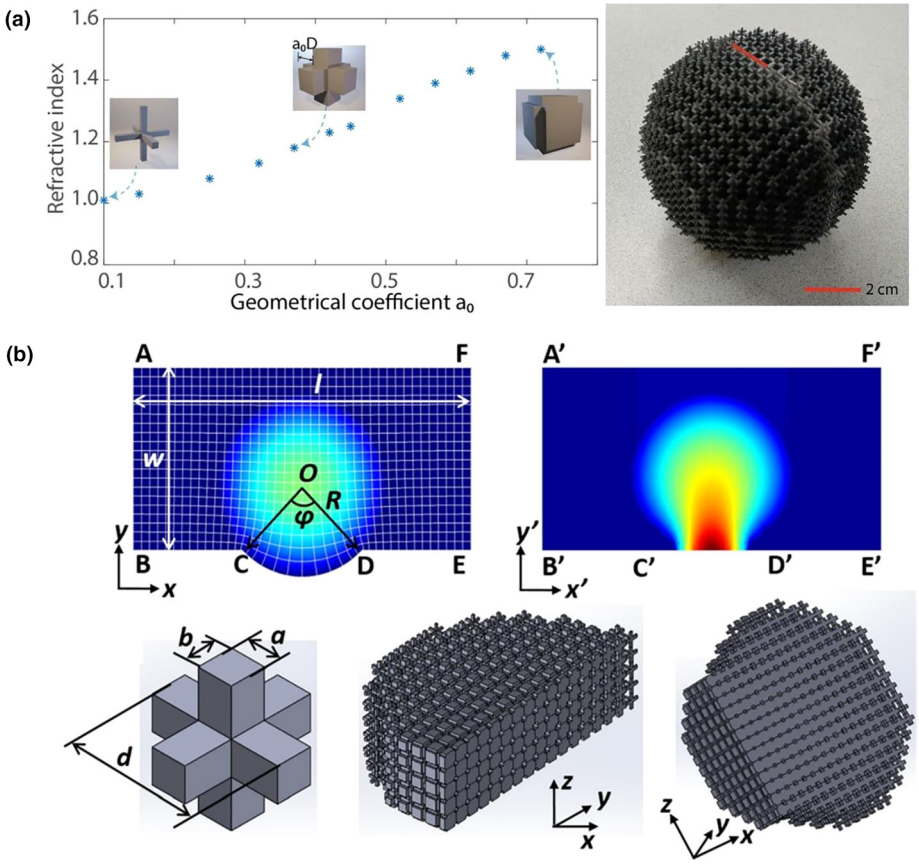

FIGURE 30

(a) Left: The building blocks of the Luneburg lens: 3D-crosses with varying geometric coefficient a0 lead to a range of refractive index. Right: A full 3D sample design for 8 kHz airborne sound. (Reprinted with permission from Ref. [238]. 2018, Springer Nature.) (b) Design of the flattened acoustic Luneburg lens. Top: Refractive index patterns for the circular acoustic Luneburg lens in the virtual space (left) and flattened acoustic Luneburg lens in physical space (right). Bottom: An example of the truss unit cell (left), the cross-sectional views of the 2D lens with five stacking layers along the *z* direction (middle) and a 3D lens with 19 stacking layers along the *z* direction (right). (Reprinted with permission from Ref. [8]. 2020, AIP Publishing.)

Typical GRIN structures are shown in Fig. 29 [231,232]. Fig. 29 (a) shows a 2D GRIN phononic crystal lens [231] by gradually rotating the scatters. The equivalent refraction index along the *y* direction was modulated to satisfy the distribution of a hyperbolic secant profile using a specific rotation angle of the scatter. By means of GRIN phononic crystal lenses, acoustic wave focusing, acoustic beam aperture modifiers, acoustic "mirage" and enhanced energy harvesting could be realized [221,224,225,233–237]. Fig. 29(b) shows an inhomogeneous acoustic metamaterial lens [232] based on the spatial variation in the refractive index for broadband focusing of underwater sound. The GRIN lens is comprised of transversely isotropic hexagonal microstructures with a tunable bulk modulus and mass density. Other examples include an acoustic Eaton lens, which could steer an acoustic wave to a desired angle [58], and a Luneburg lens [238], which is a spherically symmetrical device with unique imaging properties, as shown in Fig. 30, where different types of 3D acoustic metamaterial Luneburg lenses were applied for sound beam steering [8,238].

Prospects

After investigating dynamic mechanical metamaterials for decades, researchers can manipulate mechanical energy at will, both for the magnitude and direction of the energy flow. Mechanical energy can be dissipated, confined, redirected, or transferred to other forms of energy. Although many physical mechanisms have been well developed to achieve these functions, the manufacturing process has always lagged behind. The feature size of corresponding energy manipulation metamaterials is usually on the macroscale, which is generally bulky for application. As we can see from Fig. 2, the trade-off between the size and working frequency remains a crucial challenge, and it is still challenging to fill up the substantial blank area for small size and low-frequency applications. For example, metamaterials to shield traffic noise or seismic waves usually contain huge resonators in meter scale, which are costly and difficult to install. A possible solution is to combine different mechanisms together to obtain desired working frequencies by metamaterials with a rational geometry size.

On the other hand, with the rapid development of nanofabrication technology, we are delighted to see that phononic crystals and acoustic metamaterials at the micro- or nanoscale with an ultrahigh working frequency (GHz or THz) could be integrated into optical or thermal devices for the applications of signal processing or sensors. For example, it is possible to couple hypersonic phononic crystal [239] with other excitations, such as

Please cite this article in press as: L. Wu et al., Materials Today, (2020), https://doi.org/10.1016/j.mattod.2020.10.006

photons and electrons. The newly developed "phoxonic crystals" [240] simultaneously able to manipulate both electromagnetic and elastic wave propagation. Since the high frequency is very close to the vibration of atoms in natural crystals, and a brand-new domain might appear gradually, which combines the acoustic, optical, and even thermal domains together. Dynamic metamaterials are expected to possess more versatile and extraordinary functionalities based on the fusion of multiple fields.

Declaration of Competing Interest

The authors declare that they have no known competing financial interests or personal relationships that could have appeared to influence the work reported in this paper.

Acknowledgments

L. Wu acknowledges the Guangdong Young Talents Project under Grant No. 2018KQNCX269 and the Special Funds for the Cultivation of Guangdong College Students' Scientific and Technological Innovation under Grant No. pdjh2020b0598. Y. Wang acknowledges the National Natural Science Foundation of China under Grant Nos. 11872328, 11532011 and 11621062 and the Fundamental Research Funds for the Central Universities under Grant No. 2018FZA4025. Kuo-Chih Chuang gratefully acknowledges the financial supports from the National Natural Science Foundation of China (Grant No. 11672263 and No. 11972318). Q. Wang acknowledges the National Key Research and Development Program of China: Thirteenth Five-Year Advanced Rail Transit Key Project under Grant No. 2018YFB1201601. L. Wu and Y. Wang contributed equally to this work.

Data availability

There are no linked research data sets for this submission. The following reason is given: No data were used for the research described in the article.

References

[1] X. Yu et al., Prog. Mater Sci. 94 (2018) 114–173.
[2] D.M. Kochmann, K. Bertoldi, Appl. Mech. Rev. 69 (5) (2017).
[3] E. Barchiesi, M. Spagnuolo, L. Placidi, Math. Mech. Solids (2018). 108128651773569.
[4] J.-H. Lee, J.P. Singer, E.L. Thomas, Adv. Mater. 24 (36) (2012) 4782–4810.
[5] Q. Wang et al., Phys. Rev. Lett. 117 (17) (2016).
[6] Y. Du et al., Nano Lett. 16 (10) (2016) 6701–6708.
[7] T. Brunet, Science (2013).
[8] L. Zhao et al., Appl. Phys. Lett. 116 (7) (2020) 071902.
[9] G. Ma, P. Sheng, Sci. Adv. 2 (2) (2016) e1501595.
[10] P. Yang et al., Crystals 10 (3) (2020) 204.
[11] Y.-F. Wang et al., Compos. Struct. 206 (2018) 588–593.
[12] L. Wang et al., Adv. Mater. 23 (13) (2011) 1524–1529.
[13] L. Wu et al., Appl. Mater. Today 20 (2020) 100671.
[14] X. Fang et al., Nat. Commun. 8 (1) (2017) 1288.
[15] S.A. Cummer, J. Christensen, A. Alù, Nat. Rev. Mater. 1 (2016) 16001.
[16] P. Wang et al., Phys. Rev. Lett. 113 (1) (2014) 014301.
[17] Y. Chen, X. Liu, G. Hu, J. Sound Vib. 458 (2019) 62–73.
[18] Q.L.J.S. Vipperman, J. Vib. Acoust. 141 (2018).
[19] C. Gustavo Méndez et al., Int. J. Numer. Meth. Eng. 112 (10) (2017) 1353–1380.
[20] J. Zhu et al., J. Phys. D Appl. Phys. 48 (30) (2015) 305502.
[21] J. Zhao et al., J. Appl. Phys. 117 (21) (2015) 214507.
[22] P. Li et al., Int. J. Smart Nano Mater. 6 (1) (2015) 73–83.
[23] W. Kan et al., Phys. Rev. Appl 3 (6) (2015) 064019.
[24] C. Jo et al., Wave Motion 54 (2015) 157–169.
[25] L.-Y. Zheng et al., Appl. Phys. Lett. 104 (16) (2014) 161904.
[26] Q. Li, J.S. Vipperman, Appl. Phys. Lett. 105 (10) (2014) 101906.
[27] J. Sanchez-Dehesa et al., J. Acoust. Soc. Am. 133 (5) (2013) 3374.
[28] U. Iemma, L. Burghignoli, J. Sound Vib. 331 (21) (2012) 4629–4643.
[29] N.H. Gokhale, J.L. Cipolla, A.N. Norris, J. Acoust. Soc. Am. 132 (4) (2012) 2932–2941.
[30] X. Zhu et al., Phys. Rev. Lett. 106 (1) (2011) 014301.
[31] S. Zhang, C. Xia, N. Fang, Phys. Rev. Lett. 106 (2) (2011) 024301.
[32] D. Torrent, J. Sánchez-Dehesa, Wave Motion 48 (6) (2011) 497–504.
[33] L. Munteanu, V. Chiroiu, New J. Phys. 13 (8) (2011) 083031.
[34] V.M. García-Chocano et al., Appl. Phys. Lett. 99 (7) (2011) 074102.
[35] W. Zhu, C. Ding, X. Zhao, Appl. Phys. Lett. 97 (13) (2010) 131902.
[36] Y. Urzhumov et al., New J. Phys. 12 (7) (2010) 073014.
[37] C.L. Scandrett, J.E. Boisvert, T.R. Howarth, J. Acoust. Soc. Am. 127 (5) (2010) 2856–2864.
[38] H. Chen, C.T. Chan, J. Phys. D Appl. Phys. 43 (11) (2010) 113001.
[39] Appl. Phys. Lett. 2010, 97 (13), 131902..
[40] D. Torrent, J. Sánchez-Dehesa, New J. Phys. 10 (6) (2008) 063015.
[41] J.B. Pendry, J. Li, New J. Phys. 10 (11) (2008) 115032.
[42] A.N. Norris, Proc. Royal Soc. A 464 (2097) (2008) 2411–2434.
[43] M. Farhat et al., New J. Phys. 10 (11) (2008) 115030.
[44] M. Farhat et al., Phys. Rev. Lett. 101 (2008) 134501.
[45] S.A. Cummer et al., Phys. Rev. Lett. 100 (2) (2008) 024301.
[46] Y. Cheng et al., Appl. Phys. Lett. 92 (15) (2008) 151913.
[47] S.A. Cummer, D. Schurig, New J. Phys. 9 (3) (2007) 45.
[48] H. Chen, C.T. Chan, Appl. Phys. Lett. 91 (18) (2007) 183518.
[49] L.-W. Cai, J. Sánchez-Dehesa, New J. Phys. 9 (12) (2007) 450.
[50] X. Feng, X. Jing, Mech. Syst. Sig. Process. 117 (2019) 786–812.
[51] Y. Li et al., Appl. Phys. Lett. 111 (25) (2017) 251903.
[52] T. Jiang, Q. He, Appl. Phys. Lett. 110 (2) (2017) 021907.
[53] Z. Wang et al., Adv. Mater. 28 (44) (2016) 9857–9861.
[54] C.M. Park, S.H. Lee, Appl. Phys. Lett. 112 (7) (2018) 074101.
[55] Y. Fu et al., Phys. Rev. Mater. 2 (10) (2018).
[56] S. Tol, F.L. Degertekin, A. Erturk, Appl. Phys. Lett. 111 (1) (2017) 013503.
[57] S.H. Kim, Appl. Mech. Mater. 763 (2015) 101–104.
[58] D. Lee et al., Appl. Phys. Lett. 113 (16) (2018) 161904.
[59] M. Yin et al., Appl. Phys. Lett. 104 (9) (2014).
[60] G.S. Liu et al., Sci. Rep. 10 (1) (2020) 981.
[61] N. Geib et al., J. Acoust. Soc. Am. 145 (3) (2019) 1687.
[62] A. Song et al., Appl. Phys. A 122 (8) (2016) 759.
[63] L.-Y. Wu, L.-W. Chen, J. Appl. Phys. 110 (11) (2011) 114507.
[64] A. Khelif et al., Appl. Phys. Lett. 84 (22) (2004) 4400–4402.
[65] X. Lyu, Q. Ding, T. Yang, Appl. Math. Mech. 41 (2) (2019) 279–288.
[66] J.Y. Lee, W. Jeon, J. Acoust. Soc. Am. 141 (3) (2017) 1437.
[67] R.-Q. Cheng et al., Appl. Phys. Lett. 99 (19) (2011) 193507.
[68] B.I. Popa, L. Zigoneanu, S.A. Cummer, Phys. Rev. Lett. 106 (25) (2011) 253901.
[69] L. Zigoneanu, B.-I. Popa, S.A. Cummer, Nat. Mater. 13 (2014) 352.
[70] R.L. Harne, Y. Song, Q. Dai, Extreme Mech. Lett. 12 (2017) 41–47.
[71] J.M. Manimala, C.T. Sun, J. Appl. Phys. 115 (2) (2014) 023518.
[72] M.I. Hussein, M.J. Frazier, J. Sound Vib. 332 (20) (2013) 4767–4774.
[73] M. Molerón, M. Serra-Garcia, C. Daraio, New J. Phys. 18 (3) (2016) 033003.
[74] G.Y. Song et al., Appl. Phys. Lett. 109 (13) (2016) 131901.
[75] S. Qi et al., Appl. Phys. Lett. 108 (26) (2016) 263501.
[76] G. Ma et al., Nat. Mater. 13 (9) (2014) 873–878.
[77] L.-Y. Zheng et al., AIP Adv. 3 (10) (2013) 102122.
[78] A. Madeo et al., J. Mech. Phys. Solids 95 (2016) 441–479.
[79] N. Nejadsadeghi et al., Mech. Res. Commun. 95 (2019) 96–103.
[80] A. Madeo et al., Continuum Mech. Thermodyn. 27 (4–5) (2013) 551–570.
[81] A. Madeo et al., ZAMM – J. Appl. Math. Mech./Zeitschrift für Angewandte Mathematik und Mechanik 95 (9) (2015) 880–887.
[82] A. Madeo et al., Continuum Mech. Thermodyn. 27 (4) (2015) 551–570.
[83] I.-D. Ghiba et al., Math. Mech. Solids 20 (10) (2015) 1171–1197.
[84] G.A. Maugin, Proc. Est. Acad. Sci. A 44 (1) (1995) 12.
[85] M.G. El Sherbiny, L. Placidi, Arch. Appl. Mech. 88 (10) (2018) 1725–1742.
[86] C. Boutin, P. Roussillon, Int. J. Eng. Sci. 44 (3) (2006) 180–204.
[87] L. Jia, I. Bita, E.L. Thomas, Phys. Rev. Lett. 107 (19) (2011) 193901.
[88] H. Ünlü, Solid-State Electron. 35 (9) (1992) 1343–1352.
[89] S. John, Phys. Rev. Lett. 58 (23) (1987) 2486–2489.
[90] E. Yablonovitch, T.J. Gmitter, Phys. Rev. Lett. 63 (18) (1989) 1950–1953.
[91] S.Y. Lin et al., Nature 394 (6690) (1998) 251–253.
[92] M.M. Sigalas, E.N. Economou, J. Sound Vib. 158 (2) (1992) 377–382.
[93] M.S. Kushwaha et al., Phys. Rev. Lett. 71 (13) (1993) 2022–2025.

Please cite this article in press as: L. Wu et al., Materials Today, (2020), https://doi.org/10.1016/j.mattod.2020.10.006

[94] J.H. Lee et al., Adv. Mater. 26 (4) (2014) 532–569.
[95] E.N. Economou, M.M. Sigalas, Phys. Rev. B 48 (18) (1993) 13434–13438.
[96] J.V. Sanchez-Perez et al., Appl. Phys. Lett. 81 (27) (2002) 5240–5242.
[97] N. Aravantinos-Zafiris, M.M. Sigalas, E.N. Economou, J. Appl. Phys. 116 (13) (2014) 133503.
[98] H. Jiang et al., Appl. Phys. Lett. 95 (10) (2009) 104101.
[99] T. Miyashita, Meas. Sci. Technol. 16 (5) (2005) R47–R63.
[100] R. Martínez-Sala et al., Nature 378 (1995).
[101] L. D'Alessandro et al., Appl. Phys. Lett. 109 (22) (2016) 221907.
[102] Y. Pennec et al., Phys. Status Solidi (c) 6 (9) (2009) 2080–2085.
[103] F. Lucklum, M. Vellekoop, Crystals 7 (11) (2017) 348.
[104] S. Babaee, P. Wang, K. Bertoldi, J. Appl. Phys. 117 (24) (2015) 244903.
[105] F.-C. Hsu et al., Appl. Phys. Lett. 96 (5) (2010) 051902.
[106] S. Mohammadi et al., Appl. Phys. Lett. 92 (22) (2008) 221905.
[107] M.R. Wagner et al., Nano Lett. 16 (9) (2016) 5661–5668.
[108] S. Alaie et al., Nat. Commun. 6 (2015) 7228.
[109] M. Gorisse et al., Appl. Phys. Lett. 98 (23) (2011) 234103.
[110] Y.M. Soliman et al., Appl. Phys. Lett. 97 (19) (2010) 193502.
[111] F.R. Montero de Espinosa, E. Jiménez, M. Torres, Phys. Rev. Lett. 80 (6) (1998) 1208–1211.
[112] J.-C. Hsu, T.-T. Wu, Phys. Rev. B 74 (14) (2006).
[113] P. Zhang, A.C. To, Appl. Phys. Lett. 102 (12) (2013) 121910.
[114] D. Mousanezhad et al., Phys. Rev. B 92 (10) (2015).
[115] Y. Zhang, D. Yu, J. Wen, Extreme Mech. Lett. 12 (2017) 2–6.
[116] M. Thota, K.W. Wang, J. Appl. Phys. 122 (15) (2017) 154901.
[117] C. Goffaux, J.P. Vigneron, Phys. Rev. B 64 (7) (2001) 075118.
[118] Z. Hou, B.M. Assouar, Phys. Lett. A 372 (12) (2008) 2091–2097.
[119] J. Shim, P. Wang, K. Bertoldi, Int. J. Solids Struct. 58 (2015) 52–61.
[120] W.-P. Yang, L.-W. Chen, Smart Mater. Struct. 17 (1) (2008) 015011.
[121] J. Baumgartl, M. Zvyagolskaya, C. Bechinger, Phys. Rev. Lett. 99 (20) (2007) 205503.
[122] M.S. Kushwaha, Appl. Phys. Lett. 70 (24) (1997) 3218–3220.
[123] Z. Liu et al., Science 289 (5485) (2000) 1734–1736.
[124] C. Comi, L. Driemeier, Latin Am. J. Solids Struct. 15 (4) (2018).
[125] S. Ning et al., Extreme Mech. Lett. 35 (2020) 100623.
[126] M. Miniaci et al., Appl. Phys. Lett. 109 (7) (2016) 071905.
[127] Z. Li, X. Wang, Int. J. Solids Struct. 78–79 (2016) 174–181.
[128] M. Nouh, O. Aldraihem, A. Baz, J. Sound Vib. 341 (2015) 53–73.
[129] T. Bückmann et al., Phys. Status Solidi (b) 252 (7) (2015) 1671–1674.
[130] P.F. Pai, Int. J. Mech. Sci. (2014).
[131] M. Nouh, J. Vib. Acoust. 136 (061012) (2014).
[132] J. Hu, Int. J. Mech. Sci. (2019).
[133] H. Al Ba'ba'a, M.A. Attarzadeh, M. Nouh, J. Appl. Mech. 85 (4) (2018).
[134] C.C. Claeys, Design of a resonant metamaterial based acoustic. PROCEEDINGS OF ISMA2014 2014..
[135] D. Qi et al., Extreme Mech. Lett. 28 (2019) 58–68.
[136] F. Vadalà, ArXiv (2019).
[137] D. Beli et al., Sci. Rep. 9 (1) (2019) 5617.
[138] C. Sugino, M. Ruzzene, A. Erturk, J. Mech. Phys. Solids 116 (2018) 323–333.
[139] F. Aghighi, J. Morris, A.V. Amirkhizi, Mech. Mater. 130 (2019) 65–75.
[140] D. Beli, J.R.F. Arruda, M. Ruzzene, Int. J. Solids Struct. 139–140 (2018) 105–120.
[141] Y.Y. Chen et al., Compos. Struct. 136 (2016) 358–371.
[142] J.-S. Chen, J. Appl. Mech. (2017).
[143] J.-S. Chen et al., J. Intell. Mater. Syst. Struct. 30 (20) (2019) 2973–2981.
[144] M.A. Nouh, O.J. Aldraihem, A. Baz, J. Intell. Mater. Syst. Struct. 27 (13) (2016) 1829–1845.
[145] G. Zhou et al., Appl. Acoust. 159 (2020) 107078.
[146] Z. Li, Wave Propagation in anisotropic elastic metamaterials with broad bandgaps. CSME-CFDSC Congress 2019 2019..
[147] X. Xu et al., J. Sound Vib. (2018).
[148] L. Chenchen, dynamic behavior of elastic Metamaterials multiscale modeling, simulation, and design. thesis 2018..
[149] S.L. Sahand Sadeghi, Harnessing the Quasi-Zero Stiffness from Fluidic Origami for Low Frequency Vibration Isolation. 2017..
[150] D. Zhang, B. Ji, X. Zhou, Aerospace Systems 2 (2) (2019) 125–135.
[151] H. Yasuda, Wave dynamics in origami-based mechanical metamaterials. Thesis 2018..
[152] H. Yasuda, Origami-based impact mitigation via rarefaction solitary wave creation. arXiv:1805.05909v1 2018. arXiv:1805.05909v1 2018..
[153] H.O. Jie Liu, Rong Zeng, Miura-ori tube metamaterial with tunable dynamic property. ArXiv 2018..
[154] H. Yasuda, Tunable Wave Dynamics in Origami-Based Mechanical Metamaterials. IDETC/CIE 2016 2016..
[155] S.B. Bertoldi et al., Sci. Adv. (2016).
[156] H. Yasuda, J. Yang, J. Int. Assoc. Shell Spatial Struct. 58 (4) (2017) 287–294.
[157] R. Zhu et al., Sci. Rep. 8 (1) (2018) 483.
[158] H. Lv et al., Appl. Phys. Lett. 102 (3) (2013) 034103.
[159] D. Wu et al., Appl. Acoust. 143 (2019) 31–37.
[160] J. Hsu, K. Ahuja, Cavity noise control using Helmholtz resonators. 1996..
[161] N.S. Horioka, J. Acoust. Soc. Am. 97 (3) (1995) EL363.
[162] D.P. Elford et al., J. Acoust. Soc. Am. 130 (5) (2011) 2746–2755.
[163] Y. Zhu, B. Assouar, Phys. Rev. B 99 (17) (2019) 174109.
[164] C. Cai, C.M. Mak, J. Acoust. Soc. Am. 140 (6) (2016) EL471.
[165] J. Fey, W.M. Robertson, J. Appl. Phys. 109 (11) (2011) 114903.
[166] M.B. Xu, A. Selamet, H. Kim, Appl. Acoust. 71 (9) (2010) 822–829.
[167] R.A. Prydz et al., J. Acoust. Soc. Am. 117 (2) (1989) 725–733.
[168] N. Sugimoto, H. Imahori, J. Fluid Mech. 546 (-1) (2005) 89.
[169] N. Fang et al., Nat. Mater. 5 (6) (2006) 452–456.
[170] S.-H. Park, J. Sound Vib. 332 (20) (2013) 4895–4911.
[171] D.E. Spiel, J. Geophys. Res. 97 (C7) (1992) 11443–11452.
[172] C. Cai, C.-M. Mak, X. Shi, Appl. Acoust. 115 (2017) 74–80.
[173] F. Lemoult, M. Fink, G. Lerosey, Phys. Rev. Lett. 107 (6) (2011) 064301.
[174] J. Park et al., J. Acoust. Soc. Am. 132 (4) (2012) 2793–2799.
[175] S. Krödel, N. Thomé, C. Daraio, Extreme Mech. Lett. 4 (2015) 111–117.
[176] A. Palermo et al., Sci. Rep. 6 (2016) 39356.
[177] M. Miniaci et al., New J. Phys. 18 (8) (2016) 083041.
[178] C. Yilmaz, G.M. Hulbert, N. Kikuchi, Phys. Rev. B 76 (5) (2007).
[179] C. Yilmaz, G.M. Hulbert, Phys. Lett. A 374 (34) (2010) 3576–3584.
[180] G. Acar, C. Yilmaz, J. Sound Vib. 332 (24) (2013) 6389–6404.
[181] S. Taniker, C. Yilmaz, Int. J. Solids Struct. 72 (2015) 88–97.
[182] C. Cai et al., Compos. Struct. 236 (2020) 111862.
[183] V. Anvar, IOP Conf. Series 225 (2017) 012142.
[184] K.S. Sachiko Ishida, J. Vib. Acoust. (2017).
[185] H.H. Huang, C.T. Sun, J. Mech. Phys. Solids 59 (10) (2011) 2070–2081.
[186] M. Mohsenizadeh et al., Mater. Des. 139 (2018) 521–530.
[187] A. Rafsanjani, A. Akbarzadeh, D. Pasini, Adv. Mater. 27 (39) (2015) 5931–5935.
[188] H. Yang, L. Ma, J. Mater. Sci. 54 (4) (2018) 3509–3526.
[189] X. Tan et al., Int. J. Mech. Sci. 155 (2019) 509–517.
[190] S. Liu, A.I. Azad, R. Burgueño, Extreme Mech. Lett. 28 (2019) 1–7.
[191] C. Morris et al., Adv. Eng. Mater. 21 (7) (2019) 1900163.
[192] C. Findeisen et al., J. Mech. Phys. Solids 102 (2017) 151–164.
[193] R. Zhu, G.L. Huang, G.K. Hu, J. Vib. Acoust. (2012).
[194] M.W.U. Siddiqi, J.E. Lee, Micromachines (Basel) 9 (8) (2018).
[195] M. Badreddine Assouar et al., Ultrasonics 54 (8) (2014) 2159–2164.
[196] Y. Chen et al., Extreme Mech. Lett. 17 (2017) 24–32.
[197] V. Leroy et al., Appl. Phys. Lett. 95 (17) (2009) 171904.
[198] M. Oudich et al., New J. Phys. 12 (8) (2010) 083049.
[199] K.H. Matlack et al., Proc. Natl. Acad. Sci. 113 (30) (2016) 8386–8390.
[200] C. Nimmagadda, K.H. Matlack, J. Sound Vib. 439 (2019) 29–42.
[201] M. Badreddine Assouar, M. Oudich, Appl. Phys. Lett. 100 (12) (2012) 123506.
[202] Z. Jia et al., Phys. Rev. Appl 9 (4) (2018).
[203] Y. Chen et al., Phys. Rev. Appl 7 (2) (2017).
[204] Y. Chen, L. Wang, Appl. Phys. Lett. 105 (19) (2014) 191907.
[205] Y.A. Bogdan Ungureanu, Stefan Enoch, Auxetic like metamaterials as novel earthquake protections. ArXiv 2015..
[206] M. Oudich, M.B. Assouar, Z. Hou, Appl. Phys. Lett. 97 (19) (2010) 193503.
[207] A. Shelke et al., J. Intell. Mater. Syst. Struct. 25 (13) (2014) 1541–1552.
[208] Guided Surface Acoustic Waves in Phononic Crystal Waveguides..
[209] G.H. Li, Y.Z. Wang, Y.S. Wang, Sci. Rep. 9 (1) (2019) 16226.
[210] Y.-F. Wang et al., Phys. Rev. Appl 8 (1) (2017).
[211] Z. Tian et al., Nat. Commun. 11 (1) (2020) 762.
[212] J. Han et al., AIP Adv. 9 (6) (2019) 065201.
[213] Y. Pennec et al., Phys. Rev. E: Stat. Nonlinear Soft Matter Phys. 69 (4 Pt 2) (2004) 046608.
[214] X. Zhang, Z. Liu, Appl. Phys. Lett. 85 (2) (2004) 341–343.
[215] S. Zou et al., Phys. Rev. Lett. 123 (7) (2019) 074501.
[216] J. Hyun, W. Choi, M. Kim, Appl. Phys. Lett. 115 (17) (2019) 173901.
[217] H. Zhu, F. Semperlotti, Int. J. Smart Nano Mater. 6 (1) (2015) 1–13.
[218] S.-C.S. Lin et al., Phys. Rev. B 79 (9) (2009) 094302.
[219] A. Climente, D. Torrent, J. Sánchez-Dehesa, Appl. Phys. Lett. 105 (6) (2014) 064101.
[220] A. Climente, D. Torrent, J. Sánchez-Dehesa, Appl. Phys. Lett. 97 (10) (2010) 104103.
[221] S.-C.S. Lin et al., J. Phys. D Appl. Phys. 42 (18) (2009) 185502.
[222] D. Torrent, Y. Pennec, B. Djafari-Rouhani, J. Appl. Phys. 116 (22) (2014) 224902.

Please cite this article in press as: L. Wu et al., Materials Today, (2020), https://doi.org/10.1016/j.mattod.2020.10.006

[223] Y. Jin et al., AIP Adv. 6 (12) (2016) 121602.
[224] S.-C.S. Lin, T.J. Huang, J. Appl. Phys. 106 (5) (2009) 053529.
[225] S. Tol, F.L. Degertekin, A. Erturk, Appl. Phys. Lett. 109 (6) (2016) 063902.
[226] Y. Jin, B. Djafari-Rouhani, D. Torrent, Nanophotonics 8 (5) (2019) 685–701.
[227] Acoustically trapped colloidal crystals that are reconfigurable in real time..
[228] J. Sun, Y. Yu, In Beam focusing of surface acoustic wave using gradient-index phononic crystals, 2016 IEEE International Ultrasonics Symposium (IUS), 18-21 Sept. 2016; 2016; pp 1-3..
[229] Y. Li et al., Appl. Phys. Lett. 101 (23) (2012) 233508.
[230] J. Zhao et al., Appl. Phys. Lett. 108 (22) (2016) 221905.
[231] Y. Tian et al., J. Phys. D Appl. Phys. 52 (2) (2018) 025102.
[232] X. Su et al., J. Acoust. Soc. Am. 141 (6) (2017) 4408–4417.
[233] S. Tol, F.L. Degertekin, A. Erturk, Addit. Manuf. 29 (2019) 100780.
[234] Y. Jin et al., Nat. Commun. 10 (1) (2019) 143.
[235] S. Peng et al., Appl. Phys. Lett. 96 (26) (2010) 263502.
[236] S.-C.S. Lin, B.R. Tittmann, T.J. Huang, J. Appl. Phys. 111 (12) (2012) 123510.
[237] T.P. Martin et al., Appl. Phys. Lett. 97 (11) (2010) 113503.
[238] Y. Xie et al., Sci. Rep. 8 (1) (2018) 16188.
[239] N. Gomopoulos et al., Nano Lett. 10 (3) (2010) 980–984.
[240] Q. Rolland et al., Appl. Phys. Lett. 101 (6) (2012) 061109.

Please cite this article in press as: L. Wu et al., Materials Today, (2020), https://doi.org/10.1016/j.mattod.2020.10.006